Electronic Research Archive

ERA, 34(8): 5723–5757.
DOI: 10.3934/era.2026255
Received: 07 May 2026
Revised: 10 June 2026
Accepted: 23 June 2026
Published: 06 July 2026

https://www.aimspress.com/journal/ERA

Research article

FCTN decomposition for tensor completion with factor double sparsity regularization

Ronghuan Zhang[1,†], Yiming Zhang[2,†], Hualin Zhang[1,†] and Yingpin Chen[1,*]

[1] School of Physics and Information Engineering, Minnan Normal University, Zhangzhou 363000, China
[2] School of Life Sciences, Xiamen University, Xiamen 361000, China

† The authors contributed equally to this work.

* **Correspondence:** Email: 110500617@163.com.

Abstract: To address the performance degradation of fully connected tensor network decomposition under high missing rates, where relying solely on global low-rank priors is insufficient, we proposed a novel FCTN decomposition method based on factor double sparsity regularization, termed FCTN-FDS. The proposed method jointly incorporated gradient factor regularization and structural sparsity regularization into the FCTN framework, constraining the model at the same time from two levels: Factor representation ability and network structure, to enhance the robustness of rank selection and reduce redundant parameters. Furthermore, an efficient algorithm based on proximal alternating minimization was designed to guarantee convergence and computational efficiency. Experimental results on color image, multispectral image, and MRI recovery tasks demonstrated that the proposed method achieves superior performance in recovering fine details and complex textures compared to existing approaches, validating its effectiveness and strong representational capability.

Keywords: tensor decomposition; low rank constraint; sparsity regularization; tensor completion; Full connected tensor network

1. Introduction

With the rapid advancement of science and technology, real-world applications have increasingly generated high-dimensional complex data, such as hyperspectral images, medical imaging, and seismic data. During the acquisition of high-dimensional data, missing and corrupted elements inevitably occur due to environmental constraints, unstable imaging equipment, and other practical factors [1], which severely hinder subsequent downstream applications [2]. High-dimensional data recovery aims to accurately reconstruct intact, clean data from incomplete, noisy observations [3,4]. Its core is to leverage the latent prior knowledge embedded in the original data [5,6], thereby converting ill-posed problems into well-posed, computationally tractable ones. Common intrinsic priors include global correlation [7], local continuity [8], and nonlocal self-similarity [9,10].

Moreover, tensors have emerged to effectively characterize high-dimensional data [11]. As the high-dimensional extension of vectors and matrices, tensors possess inherent multidimensional structural properties that naturally preserve the intrinsic correlations across data modes and better represent high-dimensional data in real-world scenarios [12,13]. Nevertheless, the use of tensors for data processing also introduces the challenge of the "curse of dimensionality" [14], in which storage and computational costs increase exponentially with the growth of tensor order. This promotes the development of tensor decomposition. Through multilinear operations, high-order tensors can be decomposed into a set of low-rank latent factors, which excavate the intrinsic structure of original tensors and substantially reduce storage and computational costs. Consequently, tensor decomposition has been widely applied in numerous fields, including machine learning [15,16], computer vision [17,18], and image processing [19,20].

Classic tensor decomposition methods include CANDECOMP/PARAFAC (CP) decomposition [21,22] and Tucker decomposition [23]. These methods have achieved remarkable results in the field of data recovery. CP decomposition aims to approximately decompose a high-order tensor into the sum of R rank-one tensors. Herein, R denotes the CP rank, which is defined as the minimum number of rank-one tensors required to reconstruct the original tensor. Tucker decomposition decomposes the original tensor into the product of a core tensor and matrices of each mode, which can be regarded as high-order principal component analysis. The Tucker rank is a vector whose elements specify the rank of the unfolding matrix along the corresponding mode of the original tensor. These early methods laid the foundation for tensor decomposition, but each has its own limitations. CP decomposition enjoys a unique representation and favorable interpretability. However, determining the CP rank is an NP-hard problem [24]. CP decomposition assigns equal importance to each component across all modes, severely limiting its fitting capability for practical data and leading to unstable optimization performance. In contrast, Tucker decomposition supports mode-wise independent rank assignment, offering superior flexibility to characterize heterogeneous structural features across distinct dimensions. Nevertheless, Tucker decomposition suffers from inherent defects: The parameter scale of the core tensor grows exponentially with the tensor order, leading to prohibitive computational complexity in high-order tensor scenarios. Furthermore, matrix-based tensor unfolding destroys the intrinsic multidimensional structure, thereby failing to capture global interdependencies across unfolding modes.

To address these challenges, the tensor network (TN) theory, originally developed in condensed matter physics, has provided researchers with a novel perspective and has been introduced into computational science and signal processing [25,26]. For instance, Cichocki [27] addressed the curse of dimensionality in high-dimensional data by combining tensor networks with low-rank tensor decompositions. TN decomposition decomposes an N th-order tensor into a series of small-scale matrices/tensors (referred to as TN facts) via tensor contraction operations. The TN rank refers to a set of non-negative integer parameters that define the size of the shared dimensions connecting adjacent tensor cores. The topological structure of TN [28] can be formally formulated as a simple graph, where nodes correspond to tensor cores, and edges characterize the contraction relationships between tensors. Each elementary element of the TN rank further quantifies the weight of the corresponding edge. The tensor train (TT) decomposition, proposed by Oseledets [29], decomposes an N th-order tensor into two matrices and $N-2$ third-order tensors, featuring a "chain-like" topology. The tensor ring (TR) decomposition, proposed by Zhao et al. [30], replaces the two matrices in the TT decomposition with cyclically connected third-order tensors, decomposing an N th-order tensor into N third-order tensors and featuring a "ring-like" topology. Based on TT and TR decompositions, these methods suffer from two limitations due to constraints imposed by their inherent topological structures [31]. First, TT and TR decompositions establish multilinear operations only between adjacent cores, limiting their ability to characterize correlations within the original tensor. Second, TT decomposition is invariant only under reverse permutation of the original tensor modes, whereas TR decomposition is invariant only under circular shift permutation. Consequently, TT and TR decompositions are highly sensitive to the ordering of the original tensor modes.

In recent years, Zheng et al. [32] proposed the fully connected tensor network (FCTN) decomposition with a fully connected topological structure. Specifically, an N -order tensor is decomposed into a set of N -order factor tensors via FCTN. FCTN decomposition constructs multilinear operations between any two core tensors, which can characterize the relationships between the modes of the original tensor and better capture the global correlation of the data. In addition, FCTN decomposition exhibits permutation invariance. Nevertheless, this network structure also brings new challenges. First, the FCTN decomposition involves extensive computations of core tensors for high-order tensors, leading to high computational complexity. Second, FCTN decomposition cannot adaptively determine the tensor rank, and the FCTN rank of an N order tensor contains $N(N-1)/2$ parameters. Accordingly, it is difficult to select an appropriate FCTN rank.

Although the FCTN model exhibits remarkable advantages in characterizing the global correlation of high-order tensors, relying solely on global low-rank properties fails to yield satisfactory recovery results under extremely high missing rates. Therefore, introducing additional intrinsic priors via regularization terms plays a vital role in improving the model's stability, computational efficiency, and robustness. Among them, factor regularization imposes low-rank constraints or norm penalties on factor tensors during the optimization of FCTN decomposition. This strategy maintains the stability and sparsity of the factors, thereby reducing the risk of overfitting and enhancing the model's robustness. For instance, Zheng et al. [33] introduced a factor regularization term into the objective function to constrain the representation capability of each factor tensor. This method promotes local continuity of the target tensor, further strengthening the model's data recovery ability under high missing rates, and has achieved promising performance on tasks such as image inpainting and video restoration. On the other hand, structural sparsity regularization constrains the model from a tensor network perspective. By imposing sparse regularization constraints on tensor factor matrices, it can reduce the redundant complexity among factors and improve computational efficiency. For example, Huang et al. [34] imposed structural sparsity regularization constraints on FCTN factors. This enables the model to reduce redundant parameters while preserving tensor structural information, thereby improving the effectiveness and stability of decomposition, especially in high-dimensional data recovery tasks.

Although these regularization methods have, to some extent, addressed the challenges of rank estimation and high computational complexity in FCTN decomposition, existing approaches typically focus on a single type of regularization strategy, making it difficult to balance factor representation capability and network structure optimization simultaneously. How to effectively integrate factor and structural sparsity regularization to further enhance the algorithm's robustness and computational efficiency remains a topic worthy of in-depth investigation.

To address the aforementioned issues, we introduce gradient factor regularization and structural sparsity regularization within the FCTN decomposition framework, proposing a novel method termed FCTN-Factor Double-Sparse (FDS) (FCTN based on FDS regularization). This method imposes constraints on the model from two perspectives: Factor representation capability and FCTN network structure, thereby effectively mitigating the performance degradation problem of FCTN models while enhancing the robustness of rank selection. The major contributions of this paper are as follows:

1) We propose a novel FCTN decomposition method based on factor double-sparse regularization and establish a corresponding tensor completion model. By incorporating factor regularization and structural sparsity regularization into the FCTN framework, the proposed model effectively constrains factor complexity and reduces redundant information, thereby significantly improving the robustness of rank selection.

2) To solve the proposed model, we construct an efficient algorithm based on Proximal Alternating Minimization (PAM). This algorithm maintains high recovery accuracy while ensuring computational efficiency.

3) The effectiveness of the proposed method is validated through experiments on tasks, including color image, multispectral image, and magnetic resonance imaging (MRI) restoration. Experimental results demonstrate that the proposed method possesses superior representation capability, particularly in recovering fine details and complex textures.

2. Notations and preliminaries

2.1. Notations

In this paper, we use x, $\mathbf{x}$, $\mathbf{X}$ and $\mathcal{X}$ to denote scalars, vectors, matrices, and tensors, respectively, where scalars, vectors, and matrices can be regarded as zero-order, first-order, and second-order tensors, respectively. Given a matrix $\mathbf{X} \in \mathbb{R}^{m \times n}$, we use $\mathbf{X}^{\mathrm{T}}$, $\bar{\mathbf{X}}$, $\mathbf{X}^{\mathrm{H}}$, and $\mathbf{X}^{\dagger}$ to denote its transpose, conjugate, conjugate transpose, and Moore-Penrose pseudoinverse, respectively. Given a tensor $\mathcal{X} \in \mathbb{R}^{I_1 \times I_2 \times \cdots \times I_N}$, its $(i_1, i_2, \ldots, i_N)$-th element is denoted by $\mathcal{X}(i_1, i_2, \ldots, i_N)$, where $i_n \in [I_n]$, $n \in [N]$, and $[N]$ denote the set $\{1, 2, \ldots, N\}$. Given two N-th order tensors $\mathcal{X}$ and $\mathcal{Y}$, their inner product is defined as $\langle \mathcal{X}, \mathcal{Y} \rangle := \sum_{i_1, i_2, \ldots, i_N} \mathcal{X}(i_1, i_2, \ldots, i_N) \mathcal{Y}(i_1, i_2, \ldots, i_N)$. The Frobenius norm of a tensor $\mathcal{X}$ is denoted by $\| \mathcal{X} \|_F := \sqrt{\langle \mathcal{X}, \mathcal{X} \rangle}$. More detailed notations can be found in Table 1.

Table 1. Definitions of notations.

Notations	Explanation
x 、 $\mathbf{x}$ 、 $\mathbf{X}$ 、 $\mathcal{X}$	Scalar, vector, matrix, tensor
$\mathcal{X}(i_1,i_2,\ldots,i_N)$	The $(i_1,i_2,\ldots,i_N)$-th entry of $\mathcal{X}$
$x_{1:n}$ or $\{x_k\}_{k=1}^n$	Ordered Set $\{x_1,x_2,\cdots,x_n\}$
$\Vert\mathbf{X}\Vert_*$	Matrix nuclear norm
$\Vert\mathcal{X}\Vert_F$	Frobenius norm
$\vec{\mathcal{X}}^{\mathbf{n}}$	The tensor transpose of $\mathcal{X}$ based on $\mathbf{n}$
$\mathbf{X}_{[n_{1:d}\,\vert\,n_{d+1:N}]}$	The generalized unfolding of $\mathcal{X}$
$\mathbf{X}_{(k)}$	The mode- k unfolding of $\mathcal{X}$
$\mathbf{X}_{<k>}$	k-mode unfolding $\mathcal{X}$
$\times_{n_{1:d}}^{m_{1:d}}$	Tensor contraction
$\mathcal{X}=\mathrm{FCTN}(\{\mathcal{G}_k\}_{k=1}^N)$ and $\mathbf{r}_{\mathrm{FCTN}}$	Fully-connected tensor network decomposition and FCTN rank

2.2. Preliminaries

Definition 1 [32] (Generalized tensor transpose): Let $\mathcal{X}\in\mathbb{R}^{I_1\times I_2\times\cdots\times I_N}$ be a tensor of order N, and $\mathbf{n}=(n_1,n_2,\cdots,n_N)$ be an arbitrary permutation of $(1,2,\cdots,N)$. The tensor obtained by rearranging the pattern of $\mathcal{X}$ in the order specified by $\mathbf{n}$ is called the tensor transpose of $\mathcal{X}$ based on $\mathbf{n}$, denoted as $\vec{\mathcal{X}}^{\mathbf{n}}\in\mathbb{R}^{I_{n_1}\times I_{n_2}\times\cdots\times I_{n_N}}$. In this paper, the corresponding transpose operation and its inverse operation are represented by $\vec{\mathcal{X}}^{\mathbf{n}}=\mathrm{permute}(\mathcal{X},\mathbf{n})$ and $\mathcal{X}=\mathrm{permute}(\vec{\mathcal{X}}^{\mathbf{n}},\mathbf{n})$, respectively.

Definition 2 [32] (Generalized tensor unfolding): The generalized tensor unfolding of $\mathcal{X}$ is defined as a matrix $\mathbf{X}_{[n_{1:d}\,\vert\,n_{d+1:N}]}$ of size $\prod_{i=1}^{d}I_{n_i}\times\prod_{i=d+1}^{N}I_{n_i}$, whose elements satisfy

$$\mathbf{X}_{[n_{1:d}\vert n_{d+1:N}]}(j_1,j_2)=\mathcal{X}(i_1,i_2,\cdots,i_N), \tag{1}$$

where $j_1 = i_{n_1} + \sum_{s=2}^{d}\left((i_{n_s}-1)\prod_{m=1}^{s-1} I_{n_m}\right)$, $j_2 = i_{n_{d+1}} + \sum_{s=d+2}^{N}\left((i_{n_s}-1)\prod_{m=d+1}^{s-1} I_{n_m}\right)$. The corresponding unfolding operation and its inverse operation are represented by $\mathbf{X}_{[n_{1:d}|n_{d+1:N}]} = \text{GUnfold}(\mathcal{X}, n_{1:d} \mid n_{d+1:N})$ and $\mathcal{X} = \text{GFold}(\mathbf{X}_{[n_{1:d}|n_{d+1:N}]}, n_{1:d} \mid n_{d+1:N})$, respectively.

In this paper, $\mathbf{X}_{(k)}$ is used to represent $\mathbf{X}_{[k|1,2,\cdots,k-1,k+1,\cdots,N]}$, and this special case of $\mathcal{X}$ is called the modulo k expansion of $\mathcal{X}$. In this paper, $\mathbf{X}_{<k>}$ is used to represent $\mathbf{X}_{[1,2,\cdots,k|k+1,\cdots,N]}$, and this special case of $\mathcal{X}$ is called the k -modulo expansion of $\mathcal{X}$.

Definition 3 [32] (Tensor contraction): Let $\mathcal{X} \in \mathbb{R}^{I_1 \times I_2 \times \cdots \times I_N}$ be a tensor of order N, and $\mathcal{Y} \in \mathbb{R}^{J_1 \times J_2 \times \cdots \times J_M}$ be a tensor of order M. They satisfy $I_{n_i} = J_{m_i}$, where $i = 1, 2, \cdots, d$. Here, $\mathbf{n} = (n_1, n_2, \cdots, n_N)$ and $\mathbf{m} = (m_1, m_2, \cdots, m_M)$ are respectively a rearrangement of $(1, 2, \cdots, N)$ and $(1, 2, \cdots, M)$, satisfying $n_{d+1} < n_{d+2} < \cdots < n_N$ and $m_{d+1} < m_{d+2} < \cdots < m_M$. The tensor contraction between the $n_{1:d}$ -th mode of $\mathcal{X}$ and the $m_{1:d}$ -th mode of $\mathcal{Y}$, denoted as $\mathcal{X} \times_{n_{1:d}}^{m_{1:d}} \mathcal{Y}$, results in a tensor of order $(N + M - 2d)$

$$\mathcal{Z} = \mathcal{X} \times_{n_{1:d}}^{m_{1:d}} \mathcal{Y} \in \mathbb{R}^{I_{n_{d+1}} \times \cdots \times I_{n_N} \times J_{m_{d+1}} \times \cdots \times J_{m_M}}. \tag{2}$$

The formula for calculating its elements is

$$\begin{aligned} &\mathcal{Z}(i_{n_{d+1}}, \cdots, i_{n_N}, j_{m_{d+1}}, \cdots, j_{m_M}) = \\ &\sum_{i_{n_1}=1}^{I_{n_1}} \sum_{i_{n_2}=1}^{I_{n_2}} \cdots \sum_{i_{n_d}=1}^{I_{n_d}} \overrightarrow{\mathcal{X}}^{\mathbf{n}}(i_{n_1}, \cdots, i_{n_d}, i_{n_{d+1}}, \cdots, i_{n_N}) \overrightarrow{\mathcal{Y}}^{\mathbf{m}}(i_{n_1}, \cdots, i_{n_d}, j_{m_{d+1}}, \cdots, j_{m_M}). \end{aligned} \tag{3}$$

Definition 4 [32] (FCTN decomposition): FCTN decomposition aims to decompose a tensor $\mathcal{X} \in \mathbb{R}^{I_1 \times I_2 \times \cdots \times I_N}$ of order N into a set of factor tensors $\mathcal{G}_k \in \mathbb{R}^{R_{1,k} \times R_{2,k} \times \cdots \times R_{k-1,k} \times I_k \times R_{k,k+1} \times \cdots \times R_{k,N}}$ of order N, where $k = 1, 2, \cdots, N$, and establish the connection between any two factors. Mathematically, FCTN decomposition can be represented as

$$\mathcal{X}(i_1,i_2,\ldots,i_N)=\sum_{r_{1,2}=1}^{R_{1,2}}\sum_{r_{1,3}=1}^{R_{1,3}}\cdots\sum_{r_{N-1,N}=1}^{R_{N-1,N}}\begin{aligned}&\big(\mathcal{G}_1(i_1,r_{1,2},r_{1,3},\ldots,r_{1,N})\\&\mathcal{G}_2(r_{1,2},i_2,r_{2,3},\ldots,r_{2,N})\cdots\\&\mathcal{G}_k(r_{1,k},r_{2,k},\ldots,r_{k-1,k},i_k,r_{k,k+1},\ldots,r_{k,N})\cdots\\&\mathcal{G}_N(r_{1,N},r_{2,N},\ldots,r_{N-1,N},i_N)\big).\end{aligned}\tag{4}$$

In addition, in this paper, $\mathcal{X}=\mathrm{FCTN}(\{\mathcal{G}_k\}_{k=1}^N)$ is used to denote the FCTN decomposition, where $\{\mathcal{G}_k\}_{k=1}^N$ is the set of all FCTN factor tensors, and the FCTN rank is defined as a set of vectors

$$\mathbf{r}_{\mathrm{FCTN}}=(R_{1,2},R_{1,3},\ldots,R_{1,N},R_{2,3},R_{2,4},\ldots,R_{2,N},\ldots,R_{N-1,N})\in\mathbb{R}^{N(N-1)/2}.\tag{5}$$

Definition 5 [32] (FCTN composition): The process of generating $\mathcal{X}$ using the FCTN factor $\mathcal{G}_t\in\mathbb{R}^{R_{1,t}\times R_{2,t}\times\cdots\times R_{t-1,t}\times I_t\times R_{t,t+1}\times\cdots\times R_{t,N}}$ $t=1,2,\cdots,N$ is called FCTN composition. In addition, if one of the factors $\mathcal{G}_k$ ($k\in\{1,2,\ldots,N\}$) is excluded, it is denoted as $\mathcal{M}_k=\mathrm{FCTN}(\{\mathcal{G}_t\}_{t=1}^N,/\mathcal{G}_k)$ in this paper.

Remark 1: Assume $\mathcal{X}=\mathrm{FCTN}(\{\mathcal{G}_t\}_{t=1}^N)$ and $\mathcal{M}_k=\mathrm{FCTN}(\{\mathcal{G}_t\}_{t=1}^N,/\mathcal{G}_k)$, then the following equation holds

$$\mathbf{X}_{(k)}=\mathbf{G}_{k(k)}\mathbf{M}_{k[m_{1:N-1}|n_{1:N-1}]},\tag{6}$$

where $m_i=\begin{cases}2i, & \text{if } i<k,\\ 2i-1, & \text{if } i\ge k,\end{cases}$ $n_i=\begin{cases}2i-1, & \text{if } i<k,\\ 2i, & \text{if } i\ge k,\end{cases}$, $i=1,2,\ldots,N-1$.

Theorem 1 (Exact and fast solution of the Sylvester matrix equation [33]): Suppose that $\mathbf{A}\in\mathbb{C}^{m\times m}$ and $\mathbf{B}\in\mathbb{C}^{n\times n}$ are two matrices satisfying that $\mathbf{I}_n\otimes\mathbf{A}+\mathbf{B}^{\mathrm{T}}\otimes\mathbf{I}_m$ is invertible and the matrices $\mathbf{A}$ and $\mathbf{B}$ can be represented as $\mathbf{A}=\mathbf{U}\mathbf{\Lambda}\mathbf{U}^{\mathrm{H}}$ and $\mathbf{B}=\mathbf{V}\mathbf{\Phi}\mathbf{V}^{\mathrm{H}}$ ($\mathbf{\Lambda}\in\mathbb{C}^{m\times m}$ and $\mathbf{\Phi}\in\mathbb{C}^{n\times n}$ are diagonal matrices, $\mathbf{U}\in\mathbb{C}^{m\times m}$ and $\mathbf{V}\in\mathbb{C}^{n\times n}$ are unitary matrices), then the unique solution the Sylvester equation $\mathbf{AX}+\mathbf{XB}=\mathbf{Y}$ ($\mathbf{X}\in\mathbb{C}^{m\times n}$ and $\mathbf{Y}\in\mathbb{C}^{m\times n}$) can be fast calculated as

$$\mathbf{X}=\mathbf{U}\big((\mathbf{1}\oslash\mathbf{Q})\odot(\mathbf{U}^{\mathrm{H}}\mathbf{Y}\bar{\mathbf{V}})\big)\mathbf{V}^{\mathrm{T}},\tag{7}$$

where $\mathbf{Q}=\mathrm{repvec}(\mathrm{diag}(\mathbf{\Lambda}),n)+(\mathrm{repvec}(\mathrm{diag}(\mathbf{\Phi}),m))^{\mathrm{T}}\in\mathbb{C}^{m\times n}$, $\odot$ and $\oslash$ represent element-wise multiplication and element-wise division, respectively. The operation repvec$(\mathbf{a}, n)$ returns a $m \times n$ matrix formed by concatenating the vector $\mathbf{a}$ with the same $m \times 1$ columns side by side n times. When the input variable is a diagonal matrix, the operation diag() returns a column vector containing the elements on its main diagonal.

3. Proposed method

Real-world data typically exhibits repetitive textures and structures; consequently, it is often assumed to be low-rank. While FCTN decomposition can effectively capture global correlations in high-dimensional data, relying solely on them fails to yield satisfactory recovery when the missing rate is high. To further enhance the representation capability of FCTN decomposition, we introduce two regularization terms, gradient factor and structural sparsity regularization, and propose the FCTN-FDS decomposition. Specifically, the organization of this section is as follows: In Section 3.1, we provide a brief introduction to gradient factor regularization. In Section 3.2, we present a brief overview of structural sparsity regularization. In Section 3.3, we detail the proposed FCTN-FDS model. Finally, in Section 3.4, we describe the PAM algorithm designed for the proposed model. The technical framework of this paper is illustrated in Figure 1.

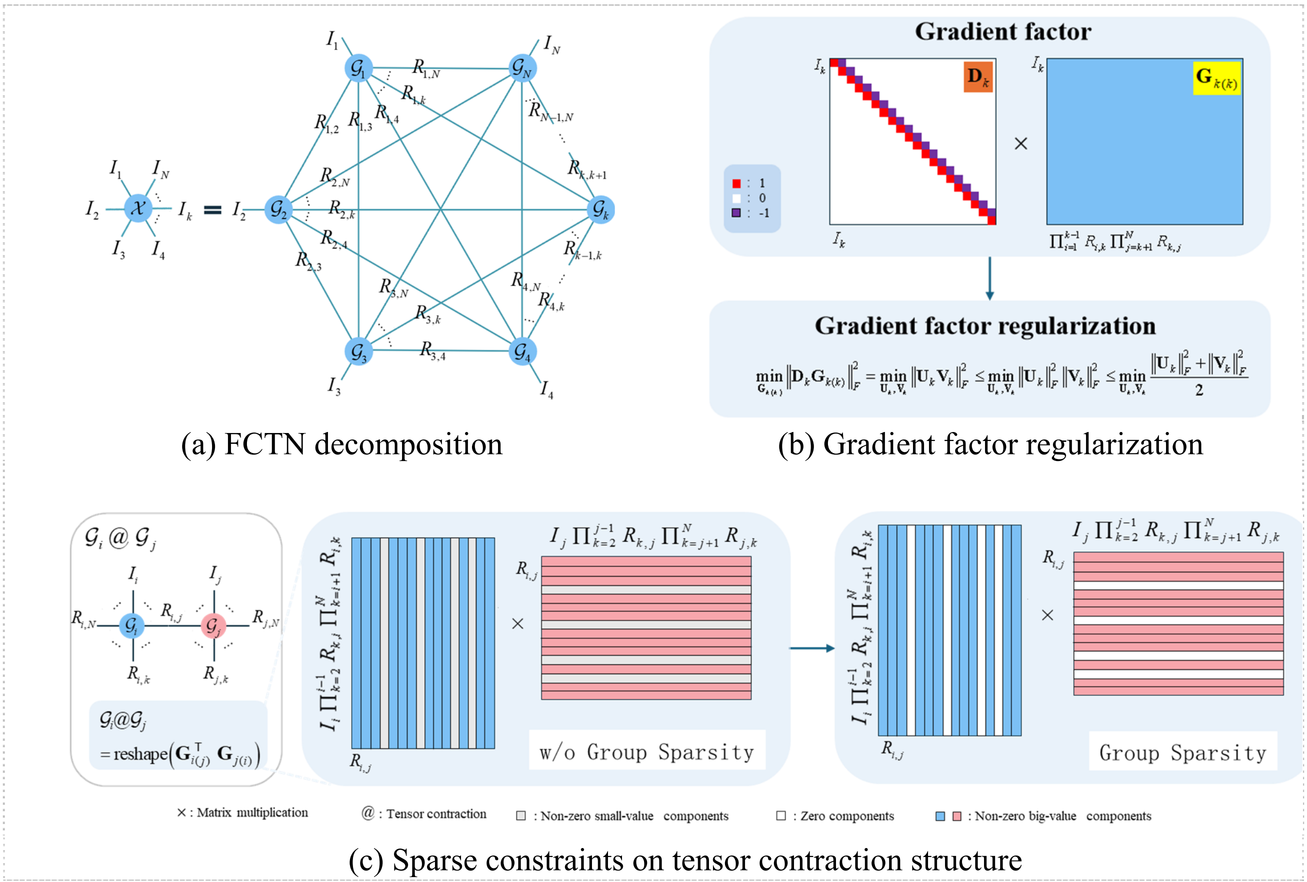

Figure 1. Schematic diagram of the FCTN-FDS technical framework.

As illustrated in Figure 1(a), there is only one common dimension between any pair of small-scale factor tensors. As illustrated in Figure 1(c), the tensor contraction between $\mathcal{G}_i$ and $\mathcal{G}_j$ is equivalent to a reshape operation following the multiplication of their corresponding unfolded matrices. However, selecting an excessively large FCTN rank results in the presence of abundant near-zero elements within the unfolded FCTN factors. These elements are the primary cause of the model's sensitivity to rank selection. To address this issue, we introduce a structural sparsity constraint. This term forces the non-structurally sparse near-zero elements in the unfolded factor matrices to shrink to exact zeros, thereby reducing the model's sensitivity to parameter selection.

3.1. Gradient factor regularization

The objective of gradient factor regularization is to incorporate prior information on local continuity into the FCTN model, thereby enhancing its ability to recover image details and textures under high missing rates. The schematic illustration is shown in Figure 1(b).

Property 1: Let $\mathcal{G}_k \in \mathbb{R}^{R_{1,k}\times R_{2,k}\times\cdots\times R_{k-1,k}\times I_k\times R_{k,k+1}\times\cdots\times R_{k,N}}$, where $k=1,2,\cdots,N$, be the FCTN factor of the N-order tensor $\mathcal{X}\in\mathbb{R}^{I_1\times I_2\times\cdots\times I_N}$, then the following inequality holds

$$\mathrm{Rank}(\mathbf{X}_{(k)}) \le \mathrm{Rank}(\mathbf{G}_{k(k)}) \le \prod\nolimits_{i=1,i\ne k}^{N} R_{k,i}, \tag{8}$$

where if $k>i$, then $R_{k,i}=R_{i,k}$.

Based on Property 1, we realize the low-rank hypothesis by assuming that the mode-k unfolding matrix $\mathbf{G}_{(k)}$ of the factor tensor is low-rank. In addition, considering that sparsity in the gradient domain is often regarded as an equivalent characterization of local continuity in the original domain, we formulate a regularization term in the gradient domain to enforce local continuity. The following difference matrix can represent the gradient operator:

$$\mathbf{D}_k = \begin{pmatrix} -1 & 1 & \dots & 0 & 0 \\ 0 & -1 & \dots & 0 & 0 \\ \vdots & \vdots & \ddots & \vdots & \vdots \\ 0 & 0 & \dots & -1 & 1 \\ 1 & 0 & \dots & 0 & -1 \end{pmatrix} \in \mathbb{R}^{I_k\times I_k}. \tag{9}$$

The rank of $\mathbf{D}_k$ is I_k-1. Therefore, we can obtain

$$\mathrm{Rank}(\mathbf{X}_{(k)}) \le \mathrm{Rank}(\mathbf{G}_{k(k)}) \le \mathrm{Rank}(\mathbf{D}_k\mathbf{G}_{k(k)})+1. \tag{10}$$

Inspired by the above analysis, we perform low-rank decomposition $\mathbf{D}_k\mathbf{G}_{k(k)}$ under the FCTN decomposition framework. Specifically, let $\mathbf{D}_k\mathbf{G}_{k(k)} = \mathbf{U}_k\mathbf{V}_k$, where $\mathbf{U}_k \in \mathbb{R}^{I_k \times r_k}$, $\mathbf{V}_k \in \mathbb{R}^{r_k \times \prod_{i=1, i\neq k}^{N} R_{k,i}}$, and in all experiments, $r_k \ll \min\{I_k, \prod_{i=1,i\neq k}^{N} R_{k,i}\}$ is set to $\max\{R_{k,1}, R_{k,2}, \ldots, R_{k,N}\}$. According to Property 1, $\prod_{i=1,i\neq k}^{N} R_{k,i}$ the upper bound of the rank of $\mathbf{X}_{(k)}$. From $\mathrm{Rank}(\mathbf{X}_{(k)}) \leq \mathrm{Rank}(\mathbf{G}_{k(k)}) \leq \mathrm{Rank}(\mathbf{D}_k\mathbf{G}_{k(k)}) + 1$, it can be seen that the low-rank decomposition of $\mathbf{D}_k\mathbf{G}_{k(k)}$ in this paper can further enhance the low-rank property of $\mathbf{X}_{(k)}$, thus improving the robustness of FCTN rank selection. In addition, we apply Tikhonov regularization to the LRMF factors $\mathbf{U}_k$ and $\mathbf{V}_k$ to promote the local continuity of the target tensor $\mathcal{X}$.

3.2. Structural sparsity regularization

Structural sparse regularization indirectly promotes the low-rankness of the target tensor by enforcing low-rankness across shared dimensions of the interaction factor unfolding matrices. Furthermore, performing zeroing operations on groups avoids information loss. In this paper, the sum of the squared Frobenius norms of the corresponding sub-factor tensors is collectively referred to as a group. The schematic illustration is shown in Figure 1(c). The detailed derivation is presented as follows:

Theorem 2 (Lemma 3 in [35]): Given a matrix $\mathbf{X} \in \mathbb{R}^{m\times n}$ with $rank(\mathbf{X}) = r \leq \min(m,n)$ and non-zero singular values σ_i $(i = 1, 2, \cdots, r)$, there exist two factor matrices $\mathbf{A} = [\mathbf{a}_1, \mathbf{a}_2, \cdots, \mathbf{a}_d] \in \mathbb{R}^{m\times d}$ and $\mathbf{B} = [\mathbf{b}_1, \mathbf{b}_2, \cdots, \mathbf{b}_d] \in \mathbb{R}^{n\times d}$, where $r \leq d \leq \min(m,n)$, such that the Schatten - 1/2 norm of $\mathbf{X}$, denoted and defined as $\|\mathbf{X}\|_{S_{1/2}}^{1/2} \triangleq \sum_{i=1}^{r} \sigma_i^{1/2}$, satisfies

$$\|\mathbf{X}\|_{S_{1/2}}^{1/2} = \min_{\mathbf{X}=\mathbf{A}\mathbf{B}^{\top}} \sum_{k=1}^{d} \sqrt{\frac{\|\mathbf{a}_k\|_2^2 + \|\mathbf{b}_k\|_2^2}{2}}, \tag{11}$$

where the equality holds when the singular value decomposition of $\mathbf{X}$ satisfies $\mathbf{X} = \mathbf{U\Sigma V}^{\mathrm{T}}$, $\mathbf{A} = \mathbf{U}\mathbf{\Sigma}^{\frac{1}{2}}$, and $\mathbf{B} = \mathbf{V}\mathbf{\Sigma}^{\frac{1}{2}}$. In addition, the extension of the above content to the tensor version is defined as follows

$$\|\mathcal{X}\|_{S_{1/2}}^{1/2} = \min_{\mathcal{X}=\mathcal{A}@\mathcal{B}} \sum_{k=1}^{d} \sqrt{\frac{\|\mathcal{A}_{:,\ldots,k,\ldots,:}\|_F^2 + \|\mathcal{B}_{:,\ldots,k,\ldots,:}\|_F^2}{2}}, \tag{12}$$

where $\mathcal{A}@\mathcal{B}$ denotes tensor contraction between $\mathcal{A}$ and $\mathcal{B}$ with one dimension.

Inspired by Theorem 2, we propose a structural sparse regularization for the tensor under the FCTN decomposition framework, which is formulated as follows

$$\mathfrak{S}(\{\mathcal{G}_k\}_{k=1}^N)=\sum_{i=1}^{N-1}\sum_{j=i+1}^{N}\sum_{r=1}^{R_{i,j}}\left(\|\mathcal{G}_i^{\{j,r\}}\|_F^2+\|\mathcal{G}_j^{\{i,r\}}\|_F^2\right)^{\frac{1}{2}}, \tag{13}$$

where $\mathcal{G}_i^{\{j,r\}}$ denotes the r -th sub-tensor of $\mathcal{G}_i$ along the j -th dimension, i.e., $\mathcal{G}_i^{\{j,r\}}=\mathcal{G}_i([1:R_{1,i}],\cdots,[1:R_{i,j-1}],r,[1:R_{i,j+1}],\cdots,[1:R_{i,N}])$. $\mathcal{G}_j^{\{i,r\}}$ is defined analogously. The first two summations correspond to the $\big(N(N-1)\big)/2$ FCTN ranks, while the remaining $\sum_{r=1}^{R_{i,j}}\left(\|\mathcal{G}_i^{\{j,r\}}\|_F^2+\|\mathcal{G}_j^{\{i,r\}}\|_F^2\right)^{\frac{1}{2}}$ reflect the structural sparsity of the unfolding matrices of $\mathcal{G}_i$ and $\mathcal{G}_j$. Minimizing the structural sparse regularization term enhances the low-rankness of the contraction result of the two factor tensors, thereby promoting the overall low-rankness of the target tensor. Specifically, structural sparse regularization induces rows or columns in the factor unfolding matrices to approach zero. Consequently, this regularization facilitates the recovery of a low-rank factor tensor without incurring the computational burden of the Singular Value Decomposition (SVD). Furthermore, pruning the corresponding near-zero rows and columns (collectively referred to as near-zero groups) can adaptively enhance the robustness of FCTN rank selection.

3.3. The proposed tensor completion model

As can be seen from Figure 1(b),(c), the gradient factor regularization and the structural sparse regularization act on the orthogonal directions of the factor tensor unfolding matrices. Therefore, the two regularization terms do not interfere with each other, avoiding the loss of important information.

Let $\mathcal{O}$ denote the partial observations of the target tensor $\mathcal{X}$. The tensor completion model proposed in this paper is formulated as follows:

$$\begin{gathered}\min_{\mathcal{X},\mathcal{G}_k,\mathbf{U}_k,\mathbf{V}_k}\|\mathcal{X}-\mathrm{FCTN}(\{\mathcal{G}_k\}_{k=1}^N)\|_F^2+\lambda_k\mathfrak{S}(\{\mathcal{G}_k\}_{k=1}^N)+\sum_{k=1}^N\beta_k(\|\mathbf{U}_k\|_F^2+\|\mathbf{V}_k\|_F^2),\\ \text{s.t. } \mathbf{D}_k\mathbf{G}_{k(k)}=\mathbf{U}_k\mathbf{V}_k,\quad \mathcal{P}_\Omega(\mathcal{X}-\mathcal{O})=0,\quad k=1,\ldots,N\end{gathered} \tag{14}$$

where $\mathcal{G}_k\in\mathbb{R}^{R_{1,k}\times R_{2,k}\times\cdots\times R_{k-1,k}\times I_k\times R_{k,k+1}\times\cdots\times R_{k,N}}$, with $k=1,2,\cdots,N$, and $\mathbf{G}_{k(k)}\in\mathbb{R}^{I_k\times\left(\prod_{i=1}^{k-1}R_{i,k}\prod_{j=k+1}^{N}R_{k,j}\right)}$ is the modulo k expansion matrix of $\mathcal{G}_k$; $\lambda>0$ is the structural sparse regularization parameter, λ represents the set $\{\lambda_1,\lambda_2,\ldots,\lambda_N\}$, $\beta_k>0$ is the gradient factor regularization parameter, $\mathbf{D}_k\in\mathbb{R}^{I_k\times I_k}$ and is the first-order difference matrix. Ω is the index of the observed elements, and let $\mathcal{P}_\Omega(\mathcal{X})$ be the projection operator. This operator preserves the elements at the observed indices while setting the remaining entries to zero.

In (14), for the regularization term $\| \mathcal{X} - \mathrm{FCTN}(\{\mathcal{G}_k\}_{k=1}^N)\|_F^2$, the global low-rankness of the target tensor is achieved by decomposing $\mathcal{X}$ into factor tensors of small dimensions. The detailed explanation of how the factor regularization term $\sum_{k=1}^{N}\beta_k(\| \mathbf{U}_k\|_F^2 + \| \mathbf{V}_k\|_F^2)$ enhances local continuity is as follows: Based on the equation $\mathbf{D}_k\mathbf{G}_{k(k)} = \mathbf{U}_k\mathbf{V}_k$, we can obtain $\| \mathbf{D}_k\mathbf{G}_{k(k)}\|_F^2 = \| \mathbf{U}_k\mathbf{V}_k\|_F^2 \le \| \mathbf{U}_k\|_F^2 \| \mathbf{V}_k\|_F^2$. Therefore, minimizing $\mathbf{U}_k$ and $\mathbf{V}_k$ can result in a smaller $\| \mathbf{D}_k\mathbf{G}_{k(k)}\|_F^2$. The local continuity of each column of $\mathbf{G}_{k(k)}$ is enhanced by left-multiplying a difference matrix $\mathbf{D}_k$ to the unfolding matrices of the factor tensors. Furthermore, since $\mathbf{X}_{(k)} = \mathbf{G}_{k(k)}\mathbf{M}_{k[m_{1:N-1}|n_{1:N-1}]}$ as stated in Remark 1, it follows that each column of $\mathbf{X}_{(k)}$ is a linear combination of the columns of $\mathbf{G}_{k(k)}$. Consequently, enhancing the local continuity of the columns of $\mathbf{G}_{k(k)}$ promotes the local continuity of the columns of $\mathbf{X}_{(k)}$. The structured sparse regularization term further enforces the low-rank structure of the precise target tensor by jointly constraining sparsity across the factor tensor network.

By introducing the indicator function of the penalty term $\min\sum_{k=1}^{N}\mu_k\| \mathbf{D}_k\mathbf{G}_{k(k)} - \mathbf{U}_k\mathbf{V}_k\|_F^2$

$$\iota_{\mathbb{S}}(\mathcal{X}) := \begin{cases} 0, & \text{if } \mathcal{X} \in \mathbb{S}, \\ \infty, & \text{otherwise}, \end{cases} \quad \text{with } \mathbb{S} := \{\mathcal{X} : \mathcal{P}_\Omega(\mathcal{X} - \mathcal{O}) = 0\}. \tag{15}$$

Applying the constraint of Eq (15) to Eq (14), we have

$$\begin{aligned} &\min_{\mathcal{X},\mathcal{G}_k,\mathbf{U}_k,\mathbf{V}_k} \| \mathcal{X} - \mathrm{FCTN}(\{\mathcal{G}_k\})\|_F^2 + \lambda_k \mathfrak{S}(\{\mathcal{G}_k\}_{k=1}^N) \\ &+ \sum_{k=1}^{N}\left(\mu_k\| \mathbf{D}_k\mathbf{G}_{k(k)} - \mathbf{U}_k\mathbf{V}_k\|_F^2 + \beta_k(\| \mathbf{U}_k\|_F^2 + \| \mathbf{V}_k\|_F^2)\right) + \iota_S(\mathcal{X}), \end{aligned} \tag{16}$$

where $\mu_k > 0$, $k = 1, 2, \cdots, N$ is the penalty parameter.

The calculation of the structured sparse regularization term $\lambda\mathfrak{S}(\{\mathcal{G}_k\}_{k=1}^N)$ involves square roots, making it difficult to minimize directly. However, by applying the inequality of arithmetic and geometric means, we obtain

$$\left(\left\|\mathcal{G}_i^{\{j,r\}}\right\|_F^2+\left\|\mathcal{G}_j^{\{i,r\}}\right\|_F^2\right)^{\frac{1}{2}} \le \frac{\frac{\left\|\mathcal{G}_i^{\{j,r\}}\right\|_F^2+\left\|\mathcal{G}_j^{\{i,r\}}\right\|_F^2}{x}+x}{2}. \tag{17}$$

For any $x>0$, the equality holds when $x=\sqrt{\left\|\mathcal{G}_i^{\{j,r\}}\right\|_F^2+\left\|\mathcal{G}_j^{\{i,r\}}\right\|_F^2}$. In Eq (16), $\mathfrak{S}(\{\mathcal{G}_k\}_{k=1}^N)=\sum_{i=1}^{N-1}\sum_{j=i+1}^{N}\sum_{r=1}^{R_{i,j}}\left(\|\mathcal{G}_i^{\{j,r\}}\|_F^2+\|\mathcal{G}_j^{\{i,r\}}\|_F^2\right)^{\frac{1}{2}} \le \sum_{i=1}^{N-1}\sum_{j=i+1}^{N}\sum_{r=1}^{R_{i,j}}\frac{\left\|\mathcal{G}_i^{\{j,r\}}\right\|_F^2+\left\|\mathcal{G}_j^{\{i,r\}}\right\|_F^2}{x}$. Therefore, we adopt an iteratively reweighted least squares strategy to solve the following model instead:

$$\begin{aligned}\min_{\mathcal{X},\mathcal{G}_k,\mathbf{U}_k,\mathbf{V}_k} & \|\mathcal{X}-\mathrm{FCTN}(\{\mathcal{G}_k\})\|_F^2+\lambda_k\sum_{i=1}^{N-1}\sum_{j=i+1}^{N}\sum_{r=1}^{R_{i,j}}\eta_r^{(i,j)}(\|\mathcal{G}_i^{\{j,r\}}\|_F^2+\|\mathcal{G}_j^{\{i,r\}}\|_F^2) \\ & +\sum_{k=1}^{N}\left(\mu_k\|\mathbf{D}_k\mathbf{G}_{k(k)}-\mathbf{U}_k\mathbf{V}_k\|_F^2+\beta_k(\|\mathbf{U}_k\|_F^2+\|\mathbf{V}_k\|_F^2)\right)+\iota_{\mathcal{S}}(\mathcal{X}),\end{aligned} \tag{18}$$

where $\eta_r^{(i,j)}=\frac{1}{x}=\frac{1}{\sqrt{\|\mathcal{G}_i^{\{j,r\}}\|_F^2+\|\mathcal{G}_j^{\{i,r\}}\|_F^2}}$.

3.4. PAM solver for the proposed model

In this subsection, we adopt the PAM framework to present the solution algorithm for the proposed model. The optimization problem in the Eq (16) can be solved by alternately updating the following system of equations:

$$\begin{cases}\mathcal{G}_k^{(s+1)}=\arg\min\limits_{\mathcal{G}_k}\|\mathcal{X}^{(s)}-\mathrm{FCTN}(\mathcal{G}_{1:k-1}^{(s+1)},\mathcal{G}_k,\mathcal{G}_{k+1:N}^{(s)})\|_F^2+\mu_k\|\mathbf{D}_k\mathbf{G}_{k(k)}-\mathbf{U}_k^{(s)}\mathbf{V}_k^{(s)}\|_F^2 \\ \qquad +\lambda_k\sum_{i=1}^{k-1}\sum_{r=1}^{R_{i,k}}\eta_r^{(i,k)}\|\mathcal{G}_k^{\{i,r\}}\|_F^2+\lambda_k\sum_{j=k+1}^{N}\sum_{r=1}^{R_{k,j}}\eta_r^{(k,j)}\|\mathcal{G}_k^{\{j,r\}}\|_F^2+\rho\|\mathcal{G}_k-\mathcal{G}_k^{(s)}\|_F^2 \\ \mathbf{U}_k^{(s+1)}=\arg\min\limits_{\mathbf{U}_k}\mu_k\|\mathbf{D}_k(\mathbf{G}_k^{(s+1)})_{(k)}-\mathbf{U}_k\mathbf{V}_k^{(s)}\|_F^2+\beta_k\|\mathbf{U}_k\|_F^2+\rho\|\mathbf{U}_k-\mathbf{U}_k^{(s)}\|_F^2 \\ \mathbf{V}_k^{(s+1)}=\arg\min\limits_{\mathbf{V}_k}\mu_k\|\mathbf{D}_k(\mathbf{G}_k^{(s+1)})_{(k)}-\mathbf{U}_k^{(s+1)}\mathbf{V}_k\|_F^2+\beta_k\|\mathbf{V}_k\|_F^2+\rho\|\mathbf{V}_k-\mathbf{V}_k^{(s)}\|_F^2 \\ \mathcal{X}^{(s+1)}=\arg\min\limits_{\mathcal{X}}\|\mathcal{X}-\mathrm{FCTN}(\{\mathcal{G}_k^{(s+1)}\}_{k=1}^N)\|_F^2+\iota_{\mathbb{S}}(\mathcal{X})+\rho\|\mathcal{X}-\mathcal{X}^{(s)}\|_F^2\end{cases}, \tag{19}$$

where $k=1,2,\cdots,N$, s is the iteration index, and $\rho>0$ is a proximal parameter. The PAM-based algorithm adopts the relative error of the reconstructed tensor between two adjacent iterations as the convergence stopping criterion, which is defined as follows:

$$\|\mathcal{X}^{(s+1)}-\mathcal{X}^{(s)}\|_F/\|\mathcal{X}^{(s)}\|_F<5\times10^{-5}. \tag{20}$$

In this paper, the tolerance is set to 5×10^{-5} to balance the fitting accuracy of tensor reconstruction and computational efficiency.

For the $\mathcal{G}_k$ sub-problem, the summation term $\sum_{r=1}^{R_{i,k}}\eta_r^{(i,k)}\|\mathcal{G}_k^{\{i,r\}}\|_F^2$ can be regarded as the weighted squared Frobenius norm of $\mathcal{G}_k$, where the weights $\sqrt{\eta_r^{(i,k)}}$ are assigned to the r-th group of $\mathcal{G}_k$ along the i-th dimension, that is $\sum_{r=1}^{R_{i,k}}\eta_r^{(i,k)}\|\mathcal{G}_k^{\{i,r\}}\|_F^2=\|\mathbf{W}^{(i,k)}\odot\mathbf{G}_{k(i)}\|_F^2$, where each column of $\mathbf{W}^{(i,k)}$ is $\left[\sqrt{\eta_1^{(i,k)}},\sqrt{\eta_2^{(i,k)}},\cdots,\sqrt{\eta_{R_{i,k}}^{(i,k)}}\right]^{\mathrm{T}}$. The same applies to $\sum_{r=1}^{R_{k,j}}\eta_r^{(k,j)}\|\mathcal{G}_k^{\{j,r\}}\|_F^2$. Since computing the derivative of the objective function in tensor form is intractable, we transform it into the following matrix form:

$$\begin{aligned}\mathcal{G}_k^{(s+1)}=\arg\min_{\mathcal{G}_k}\|\mathbf{X}_{(k)}^{(s)}-\mathbf{G}_{k(k)}\mathbf{M}_k^{(s)}\|_F^2+\lambda_k\sum_{i=1}^{k-1}\left\|\widehat{\mathbf{W}}^{(i,k)}\odot\mathbf{G}_{k(k)}\right\|_F^2+\lambda_k\sum_{j=k+1}^{N}\left\|\widehat{\mathbf{W}}^{(k,j)}\odot\mathbf{G}_{k(k)}\right\|_F^2\\+\mu_k\|\mathbf{D}_k\mathbf{G}_{k(k)}-\mathbf{U}_k^{(s)}\mathbf{V}_k^{(s)}\|_F^2+\rho\|\mathbf{G}_{k(k)}-(\mathbf{G}_k^{(s)})_{(k)}\|_F^2,\end{aligned}\tag{21}$$

where $\mathbf{M}_k^{(s)}=\mathrm{GUnfold}(\mathcal{M}_k^{(s)},\mathbf{m}\,|\,\mathbf{n})$, $\mathcal{M}_k^{(s)}=\mathrm{FCTN}(\mathcal{G}_{1:k-1}^{(s+1)},\mathcal{G}_k,\mathcal{G}_{k+1:N}^{(s)},/\mathcal{G}_k)$, and the vectors $\mathbf{m}$ and $\mathbf{n}$ are set the same as in Remark 1; $\widehat{\mathbf{W}}^{(i,k)}$ is reshaped from $\mathbf{W}^{(i,k)}$ via the transformation from $(\mathbf{G}_k)_{(i)}$ to $(\mathbf{G}_k)_{(k)}$, specifically involving mode-i folding and mode-k unfolding, for $i=1,2,\ldots$, $k-1$. The same applies to $\widehat{\mathbf{W}}^{(k,j)}$ for $j=k+1,\ldots,N$. Since all columns of $\mathbf{W}^{(i,k)}$ are identical, all rows of $\widehat{\mathbf{W}}^{(i,k)}$ are also identical. We utilize this common row vector to construct a diagonal matrix $\Lambda^{(i,k)}$ by placing the vector along the diagonal. Consequently, we have the relationship $\widehat{\mathbf{W}}^{(i,k)}\odot(\mathbf{G}_k)_{(k)}=(\mathbf{G}_k)_{(k)}\mathbf{\Theta}^{(i,k)}$. Equation (21) is differentiable; therefore, its solution can be obtained by solving the following Sylvester matrix equation, which is calculated by setting

$$\frac{\partial\left(\begin{aligned}\|\mathbf{X}_{(k)}^{(s)}-\mathbf{G}_{k(k)}\mathbf{M}_k^{(s)}\|_F^2+\lambda_k\sum_{i=1}^{k-1}\left\|\widehat{\mathbf{W}}^{(i,k)}\odot\mathbf{G}_{k(k)}\right\|_F^2+\lambda_k\sum_{j=k+1}^{N}\left\|\widehat{\mathbf{W}}^{(k,j)}\odot\mathbf{G}_{k(k)}\right\|_F^2\\+\mu_k\|\mathbf{D}_k\mathbf{G}_{k(k)}-\mathbf{U}_k^{(s)}\mathbf{V}_k^{(s)}\|_F^2+\rho\|\mathbf{G}_{k(k)}-(\mathbf{G}_k^{(s)})_{(k)}\|_F^2\end{aligned}\right)}{\partial\mathbf{G}_{k(k)}}=\mathbf{0}$$, that is

$$\begin{aligned}\mathbf{G}_{k(k)}\mathbf{M}_k^{(s)}(\mathbf{M}_k^{(s)})^{\mathrm{T}}+\lambda_k\left(\sum_{i=1}^{k-1}\mathbf{G}_{k(k)}(\mathbf{\Theta}^{(i,k)})^2+\sum_{j=k+1}^{N}\mathbf{G}_{k(k)}(\mathbf{\Theta}^{(k,j)})^2\right)\\+\mu_k\mathbf{D}_k^{\mathrm{T}}\mathbf{D}_k\mathbf{G}_{k(k)}+\rho\mathbf{G}_{k(k)}=\mathbf{X}_{(k)}^{(s)}(\mathbf{M}_k^{(s)})^{\mathrm{T}}+\mu_k\mathbf{D}_k^{\mathrm{T}}\mathbf{U}_k^{(s)}\mathbf{V}_k^{(s)}+\rho(\mathbf{G}_k^{(s)})_{(k)}.\end{aligned}\tag{22}$$

Furthermore, the diagonalization of $\mathbf{M}_k^{(s)}(\mathbf{M}_k^{(s)})^{\mathrm{T}}+\lambda_k\sum_{i=1}^{k-1}(\boldsymbol{\Theta}^{(i,k)})^2+\lambda_k\sum_{j=k+1}^{N}(\boldsymbol{\Theta}^{(k,j)})^2$ and $\mathbf{D}_k^{\mathrm{T}}\mathbf{D}_k$ is realized by means of eigenvalue decomposition and one-dimensional Fast Fourier Transform, respectively. Consequently, we obtain

$$\begin{cases}\mathbf{M}_k^{(s)}(\mathbf{M}_k^{(s)})^{\mathrm{T}}+\lambda_k\sum_{i=1}^{k-1}(\boldsymbol{\Theta}^{(i,k)})^2+\lambda_k\sum_{j=k+1}^{N}(\boldsymbol{\Theta}^{(k,j)})^2=\mathbf{P\Phi P}^{\mathrm{T}}\\ \mathbf{D}_k^{\mathrm{T}}\mathbf{D}_k=\mathbf{F}^{\mathrm{H}}\boldsymbol{\Lambda}\mathbf{F}\end{cases}, \tag{23}$$

where $\boldsymbol{\Lambda}=\operatorname{diag}\left((\varepsilon_1,\varepsilon_2,\ldots,\varepsilon_{q_k})^{\mathrm{T}}\right)\in\mathbb{R}^{q_k\times q_k}$, $\boldsymbol{\Phi}=\operatorname{diag}\left((\xi_1,\xi_2,\ldots,\xi_{p_k})^{\mathrm{T}}\right)\in\mathbb{R}^{p_k\times p_k}$, and ξ_i ($i=1,2,\ldots,p_k$) is the eigenvalue of $\mathbf{M}_k^{(s)}(\mathbf{M}_k^{(s)})^{\mathrm{T}}+\lambda_k\sum_{i=1}^{k-1}(\boldsymbol{\Theta}^{(i,k)})^2+\lambda_k\sum_{j=k+1}^{N}(\boldsymbol{\Theta}^{(k,j)})^2$, and $\mathbf{P}\in\mathbb{R}^{p_k\times p_k}$ is an orthogonal matrix, whose i-th column corresponds to the real eigenvector $\mathbf{p}_i$ of the eigenvalue ξ_i. ε_j ($j=1,2,\ldots,q_k$) is the eigenvalue of $\mathbf{D}_k^{\mathrm{T}}\mathbf{D}_k$, and $\mathbf{F}\in\mathbb{C}^{q_k\times q_k}$ denotes the one-dimensional discrete Fourier transform matrix, which is a unitary matrix.

Based on Theorem 1, the closed-form solution to the Sylvester matrix equation in Eq (22) is derived as follows:

$$\begin{aligned}&(\mathbf{G}_k)_{(k)}^{(s+\frac{1}{2})}=\mathbf{F}^{\mathrm{H}}\big((\mathbf{1}\oslash\mathbf{Q})\odot(\mathbf{FKP})\big)\mathbf{P}^{\mathrm{T}}\\&\mathcal{G}_k^{(s+\frac{1}{2})}=\operatorname{GFold}\big((\mathbf{G}_k)_{(k)}^{(s+\frac{1}{2})},k\,|\,1,\ldots,k-1,k+1,\ldots,N\big),\end{aligned}\tag{24}$$

where $\mathbf{Q}=\mu_k\operatorname{repvec}(\operatorname{diag}(\boldsymbol{\Lambda}),p_k)+(\operatorname{repvec}(\operatorname{diag}(\boldsymbol{\Phi}),I_k))^{\mathrm{T}}+\rho\operatorname{ones}(I_k,p_k)$, $\mathbf{K}=\mathbf{X}_{(k)}^{(s)}(\mathbf{M}_k^{(s)})^{\mathrm{T}}+\mu_k\mathbf{D}_k^{\mathrm{T}}\mathbf{U}_k^{(s)}\mathbf{V}_k^{(s)}+\rho(\mathbf{G}_k^{(s)})_{(k)}$; the operation $\operatorname{ones}(I_1,I_2,\ldots,I_N)$ returns a tensor of size $I_1,I_2,\ldots,I_N$ with all elements being 1.

After solving for $\mathcal{G}_k^{(s+\frac{1}{2})}$, we shrink the near-zero elements in the FCTN factors to zero. As shown in Figure 1(c), after performing the $\mathcal{G}_i@\mathcal{G}_j=\operatorname{reshape}(\mathbf{G}_{i(j)}^{\mathrm{T}}\mathbf{G}_{j(i)})$ shrinkage operation, a large number of near-zero elements exist in the FCTN factor unfolding matrices. In this paper, we employ a rank-elimination operator to directly shrink near-zero elements in $\mathbf{G}_{i(j)}^{\mathrm{T}}$ and $\mathbf{G}_{j(i)}$ to zero. We define a threshold α; if the column sum $\mathbf{G}_{i(j)}^{\mathrm{T}}$ is lower than this threshold, the column is set to zero. Similarly, if the row sum $\mathbf{G}_{j(i)}$ is below the threshold τ, the row is cleared.

$$\left(\mathcal{G}_i^{(s+1)},\mathcal{G}_j^{(s+1)}\right)=\mathrm{RankE}(\mathcal{G}_i^{(s+\frac{1}{2})},\mathcal{G}_j^{(s+\frac{1}{2})},\tau), \tag{25}$$

where $i=1,2,\cdots N-1$, $j=i+1,\cdots,N$, and RankE is the rank-elimination operator.

After updating $\mathcal{G}_k$, the weights are updated according to the following equation

Algorithm 1: FCTN-FDS

1. Input: Observation tensor $\mathcal{O}\in\mathbb{R}^{I_1\times I_2\times..\times I_N}$, indices of known elements Ω, maximum value of FCTN rank $\mathbf{r}_{\mathrm{FCTN}}^{\max}$, parameters λ_k, β_k, μ_k, $\rho=0.1$, and $s_{\max}$, initial target tensor $\mathcal{X}^{(0)}=\mathcal{O}$, and initial factor tensor $\mathcal{G}_k^{(0)}=\mathrm{rand}(R_{1,k},R_{2,k},\ldots,R_{k-1,k},I_k,R_{k,k+1},\ldots,R_{k,N})$, $r_k=\max\{R_{1,k},R_{2,k},\ldots,R_{k-1,k},R_{k,k+1},\ldots,R_{k,N}\}$, $\mathbf{U}_k^{(0)}=\mathrm{rand}(I_k,r_k)$, $\mathbf{V}_k^{(0)}=\mathrm{rand}\left(r_k,\prod_{i=1}^{k-1}R_{i,k}\prod_{j=k+1}^{N}R_{k,j}\right)$ where $k=1,2,\cdots,N$;
2. **For** $s=1:s_{\max}$
3. Update $\mathcal{G}_k^{(s+\frac{1}{2})}$ by Eq (24);
4. Update $\mathcal{G}_k^{(s+1)}$ by Eq (25);
5. Update $\eta_r^{(i,k)}$ and $\eta_r^{(k,j)}$ by Eq (26);
6. Update $\mathbf{U}_k$ by Eq (28);
7. Update $\mathbf{V}_k$ by Eq (30);
8. Update $\mathcal{X}$ by Eq (31);
9. **If** $\|\mathcal{X}^{(s+1)}-\mathcal{X}^{(s)}\|_F/\|\mathcal{X}^{(s)}\|_F<5\times10^{-5}$:
10. **break**;
11. **End For.**
12. Output: Reconstructed tensor $\mathcal{X}$.

$$\begin{cases} \eta_r^{(i,k)} = \dfrac{1}{\sqrt{\| \mathcal{G}_i^{\{k,r\}} \|_F^2 + \| \mathcal{G}_k^{\{i,r\}} \|_F^2}} \\ \eta_r^{(k,j)} = \dfrac{1}{\sqrt{\| \mathcal{G}_k^{\{j,r\}} \|_F^2 + \| \mathcal{G}_j^{\{k,r\}} \|_F^2}} \end{cases}, \tag{26}$$

where $r = 1, 2, \ldots, R_{i,k}$.

By setting

$$\begin{aligned} &\frac{\partial \left(\mu_k \| \mathbf{D}_k (\mathbf{G}_k^{(s+1)})_{(k)} - \mathbf{U}_k \mathbf{V}_k^{(s)} \|_F^2 + \beta_k \| \mathbf{U}_k \|_F^2 + \rho \| \mathbf{U}_k - \mathbf{U}_k^{(s)} \|_F^2 \right)}{\partial \mathbf{U}_k} \\ &= 2\mu_k \left(\mathbf{U}_k \mathbf{V}_k^{(s)} - \mathbf{D}_k (\mathbf{G}_k^{(s+1)})_{(k)} \right) \left(\mathbf{V}_k^{(s)} \right)^{\mathrm{T}} + 2\beta_k \mathbf{U}_k + 2\rho \left(\mathbf{U}_k - \mathbf{U}_k^{(s)} \right) = \mathbf{0}, \end{aligned} \tag{27}$$

$\mathbf{U}_k$ can be obtained

$$\mathbf{U}_k^{(s+1)} = \left(\mu_k \mathbf{D}_k (\mathbf{G}_k^{(s+1)})_{(k)} (\mathbf{V}_k^{(s)})^{\mathrm{T}} + \rho \mathbf{U}_k^{(s)} \right) \left(\mu_k \mathbf{V}_k^{(s)} (\mathbf{V}_k^{(s)})^{\mathrm{T}} + (\beta_k + \rho) \mathbf{I}_{r_k} \right)^{-1}. \tag{28}$$

By setting

$$\begin{aligned} &\frac{\partial \left(\mu_k \| \mathbf{D}_k (\mathbf{G}_k^{(s+1)})_{(k)} - \mathbf{U}_k^{(s+1)} \mathbf{V}_k \|_F^2 + \beta_k \| \mathbf{V}_k \|_F^2 + \rho \| \mathbf{V}_k - \mathbf{V}_k^{(s)} \|_F^2 \right)}{\partial \mathbf{V}_k} \\ &= \left(\mathbf{U}_k^{(s+1)} \right)^{\mathrm{T}} \left(\mathbf{U}_k^{(s+1)} \mathbf{V}_k - \mathbf{D}_k (\mathbf{G}_k^{(s+1)})_{(k)} \right) + 2\beta_k \mathbf{V}_k + 2\rho \left(\mathbf{V}_k - \mathbf{V}_k^{(s)} \right) = \mathbf{0}, \end{aligned} \tag{29}$$

$\mathbf{V}_k$ can be obtained

$$\mathbf{V}_k^{(s+1)} = \left(\mu_k (\mathbf{U}_k^{(s+1)})^{\mathrm{T}} \mathbf{U}_k^{(s+1)} + (\beta_k + \rho) \mathbf{I}_{r_k} \right)^{-1} \left(\mu_k (\mathbf{U}_k^{(s+1)})^{\mathrm{T}} \mathbf{D}_k (\mathbf{G}_k^{(s+1)})_{(k)} + \rho \mathbf{V}_k^{(s)} \right). \tag{30}$$

$\mathcal{X}$ can be obtained

$$\mathcal{X}^{(s+1)} = \mathcal{P}_{\Omega} \left(\frac{\mathrm{FCTN}\left(\{\mathcal{G}_k^{(s+1)}\}_{k=1}^N \right) + \rho \mathcal{X}^{(s)}}{1+\rho} \right) + \mathcal{P}_{\Omega}(\mathcal{O}). \tag{31}$$

Finally, the pseudo-code of the proposed model based on the PAM optimization algorithm is summarized in Algorithm 1.

3.5. Computational complexity analysis

For notational simplicity, we assume that the input N-order tensor $\mathcal{X}$ has a size of $I \times I \times I \times \cdots \times I$ and an FCTN rank of $(R \times R \times R \times \cdots \times R) \in \mathbb{R}^{\frac{N(N-1)}{2}}$. As shown in Algorithm 1, the computational cost is primarily composed of the update operations for four components: $\mathcal{G}_k$, $\mathcal{X}$, $\mathbf{U}_k$, and $\mathbf{V}_k$. Specifically, updating $\mathcal{G}_k$ via (25) involves FCTN factor, matrix eigenvalue decomposition, 1D FFT, matrix multiplication, component-wise multiplication, and component-wise division, which incur computational costs of $\mathcal{O}\left(\sum_{k=2}^{N-1} I^k R^{k(N-k)+k-1}\right)$, $\mathcal{O}\left(R^{3(N-1)}\right)$, $\mathcal{O}\left(\left(I^2+IR^{N-1}\right)\log I\right)$, $\mathcal{O}\left(I^{N-1}R^{2(N-1)}+(N-1)R^{N-1}+I^3+I^N R^{N-1}\right)$, $\mathcal{O}\left(IR^{N-1}\right)$, and $\mathcal{O}\left(IR^{N-1}\right)$, respectively. Moreover, the cost of updating $\mathcal{X}$ via (31) is $\mathcal{O}\left(\sum_{k=2}^{N-1} I^k R^{k(N-k)+k-1}\right)$. Additionally, the computational cost of updating $\mathbf{U}_k$ through (28) is $\mathcal{O}\left(I^2 R^{N-1}\right)$. Thus, updating $\mathbf{V}_k$ via (30) incurs a cost of $\mathcal{O}\left(I^2 R+IR^N\right)$. Therefore, the total computational complexity of Algorithm 1 per iteration is $\mathcal{O}\left(\sum_{k=2}^{N-1} I^k R^{k(N-k)+k-1}+N(N-1)R^{N-1}+NI^{N-1}R^{2(N-1)}+NI^3\right)$.

4. Experiments

4.1. Experiment description

In this section, we comprehensively evaluate the performance of the proposed FCTN-FDS on representative high-dimensional data recovery tasks. The experiments are conducted on color images, multispectral images (MSI), and magnetic resonance imaging (MRI) datasets. We adopt a random sampling strategy to obtain incomplete observations from the data. Typically, the sampling ratio (SR) is defined as the proportion of observed entries to the total number of entries. The competing methods in this paper include: the Tucker decomposition-based method (Tmac [36]), the t-SVD-based methods (TNN [37], METNN [38], 3DLogTNN [39]), the TR decomposition-based methods (TRGFR [8], TRLRF [40]), and the FCTN decomposition-based methods (FCTN [32], FCTNFR [33], FCTNGS [34]). It is worth noting that, for third-order data, the FCTN decomposition is essentially equivalent to the TR decomposition. Since they share the same topological structure, their performance is identical. To objectively evaluate the performance of different methods, we use the Peak Signal-to-Noise Ratio (PSNR) and the Structural Similarity Index Measure (SSIM) as image quality metrics. Generally, higher values of PSNR and SSIM indicate better quality of the recovered images.

In each experiment, all methods utilize only a single incomplete observation as training data. The hyperparameters of the competing methods are adjusted according to the source codes provided in the corresponding literature. For the proposed method, the parameters are set as follows in all experiments: $N=3$. The parameters β_k, λ_k, and μ_k are uniformly set to 0.5, 0.01, and 1, respectively, for $k=1,2,3$. The threshold τ is set to 0.001, and the proximal parameter ρ is set to 0.1. All experiments are conducted on a 14-inch MacBook Pro equipped with an Apple M5 chip, 32 GB of unified memory, and an Apple M5 integrated GPU. All methods are implemented using MATLAB

R2025b.

4.2. Color image completion

In this subsection, we present the experimental results for six color images (Castle, Mushroom, Human, Steeple, Pottery, and Water) from three aspects: quantitative evaluation, qualitative evaluation, and graffiti removal applications. The test images are shown in Figure 2. In the color image completion experiments, each image is resized to a spatial resolution of 256 × 256 pixels with three color channels (RGB). The number of iterations for each algorithm is set to 200. We employ PSNR and SSIM as metrics to evaluate the quality of the recovery results.

Figure 2. Test image. (a) Castle; (b) Mushroom; (c) Human; (d) Steeple; (e) Pottery; (f) Water.

4.2.1. Color image reconstruction under random uniform data missing

For random missing experiments on color images, we present results for three test images: Castle, Mushroom, and Human. The missing rate (MR) is set to 20%, 30%, 40%, 50%, 60%, 70%, 80%, and 90%. Tables 2 and 3 list the quantitative recovery results (PSNR and SSIM) of the restored color images. The best, second-best, and third-best results are highlighted in bold red, bold blue, and bold green, respectively. The proposed FCTN-FDS achieves superior recovery across all images and missing rates, demonstrating strong generalization in various scenarios. These quantitative results indicate that the proposed FCTN-FDS possesses powerful representation capability in recovering these color images.

Table 2. PSNR results (dB) of different methods for color image completion.

Image	Method	MR							
		20%	30%	40%	50%	60%	70%	80%	90%
Castle	Tmac	39.66	36.38	33.58	31.08	28.67	26.20	23.11	18.00
	TNN	45.35	39.76	35.98	32.61	29.41	26.75	23.75	20.20
	3DLogTNN	45.21	40.90	37.74	34.31	31.89	**29.28**	**26.38**	17.06
	METNN	45.05	40.05	36.56	33.17	29.93	27.22	24.28	19.00
	TRLRF	41.85	38.47	35.50	32.57	29.69	27.10	24.48	21.61
	TRGFR	**45.54**	**41.54**	**38.51**	**35.29**	**32.34**	29.07	26.28	**23.10**
	FCTN	40.12	36.99	33.76	31.42	28.93	26.11	23.20	19.61
	FCTNFR	**46.82**	**41.80**	**38.75**	**35.16**	**32.04**	**29.35**	**26.81**	**23.27**
	FCTNGS	40.89	37.04	34.40	31.72	29.30	26.74	24.48	20.85
	FCTN-FDS	**46.84**	**41.95**	**38.96**	**35.48**	**32.49**	**29.77**	**27.13**	**23.57**
Mushroom	Tmac	41.58	38.35	35.40	32.25	29.45	27.15	24.25	18.56
	TNN	45.18	40.16	36.08	32.82	29.70	26.89	24.24	20.59
	3DLogTNN	**49.74**	**45.94**	**42.69**	**39.62**	**36.67**	**33.61**	**30.17**	**26.06**
	METNN	45.33	41.05	37.27	34.08	30.88	27.94	25.21	20.81
	TRLRF	42.51	39.49	36.51	33.80	30.99	28.25	25.66	22.74
	TRGFR	45.72	42.60	39.78	36.65	33.90	30.61	**27.82**	24.72
	FCTN	39.69	36.91	33.78	31.77	29.22	26.82	23.92	20.71
	FCTNFR	**47.79**	**44.18**	**40.64**	**36.99**	**33.97**	**30.71**	27.79	**24.84**
	FCTNGS	39.71	37.14	33.84	31.82	29.48	27.10	25.10	22.19
	FCTN-FDS	**47.92**	**44.33**	**40.77**	**37.38**	**34.30**	**31.09**	**28.25**	**25.24**
Human	Tmac	39.76	36.62	33.74	31.04	28.66	26.29	23.85	17.55
	TNN	**45.01**	39.82	35.56	32.39	29.25	26.46	23.89	20.40
	3DLogTNN	16.79	15.65	14.57	13.72	12.76	11.97	11.13	9.79
	METNN	44.83	40.19	36.35	33.25	29.97	27.17	24.29	18.19
	TRLRF	40.83	37.99	35.09	32.38	29.55	27.03	24.76	22.09
	TRGFR	44.85	**41.12**	**38.00**	**35.29**	**32.53**	**29.70**	**27.06**	**23.96**
	FCTN	38.88	36.01	33.05	30.97	28.83	25.88	22.93	19.91
	FCTNFR	**47.34**	**42.78**	**39.23**	**35.90**	**32.50**	**29.73**	**27.27**	**23.91**
	FCTNGS	39.09	36.35	33.13	31.12	28.54	26.39	24.29	21.17
	FCTN-FDS	**47.25**	**42.79**	**39.50**	**35.98**	**32.87**	**30.09**	**27.46**	**24.21**

Table 3. SSIM results of different methods for color image completion.

Image	Method	MR							
		20%	30%	40%	50%	60%	70%	80%	90%
Castle	Tmac	0.9819	0.9648	0.9388	0.9047	0.8564	0.7948	0.6646	0.3217
	TNN	0.9957	0.9874	0.9707	0.9429	0.8937	0.8242	0.7031	0.4975
	3DLogTNN	**0.9980**	**0.9951**	**0.9900**	**0.9795**	**0.9612**	**0.9268**	**0.8386**	0.3606
	METNN	0.9956	0.9890	0.9763	0.9532	0.9090	0.8441	0.7368	0.4558
	TRLRF	0.9888	0.9793	0.9623	0.9363	0.8941	0.8315	0.7373	0.5881
	TRGFR	0.9962	**0.9926**	**0.9854**	0.9740	**0.9547**	0.9152	**0.8516**	**0.7108**
	FCTN	0.9833	0.9693	0.9442	0.9134	0.8660	0.7876	0.6581	0.4281
	FCTNFR	**0.9967**	0.9925	0.9831	**0.9666**	0.9385	**0.8949**	0.8296	**0.6679**
	FCTNGS	0.9841	0.9699	0.9532	0.9246	0.8849	0.8193	0.7372	0.5528
	FCTN-FDS	**0.9966**	**0.9927**	**0.9840**	**0.9692**	**0.9446**	**0.9039**	**0.8416**	**0.7030**
Mushroom	Tmac	0.9843	0.9664	0.9396	0.8862	0.8070	0.7182	0.5673	0.2780
	TNN	0.9945	0.9828	0.9603	0.9219	0.8527	0.7507	0.6140	0.4079
	3DLogTNN	**0.9985**	**0.9967**	**0.9935**	**0.9873**	**0.9746**	**0.9494**	**0.8909**	**0.7353**
	METNN	0.9947	0.9859	0.9693	0.9392	0.8798	0.7804	0.6585	0.4243
	TRLRF	0.9877	0.9751	0.9557	0.9229	0.8662	0.7798	0.6586	0.4712
	TRGFR	0.9952	0.9902	0.9820	0.9665	**0.9396**	**0.8850**	**0.8000**	**0.6264**
	FCTN	0.9770	0.9558	0.9204	0.8803	0.8095	0.7136	0.5567	0.3311
	FCTNFR	**0.9967**	**0.9923**	**0.9820**	**0.9662**	0.9309	0.8690	0.7779	0.6249
	FCTNGS	0.9774	0.9567	0.9223	0.8662	0.8111	0.7190	0.6282	0.4418
	FCTN-FDS	**0.9968**	**0.9928**	**0.9849**	**0.9697**	**0.9375**	**0.8821**	**0.7983**	**0.6520**
Human	Tmac	0.9795	0.9595	0.9268	0.8766	0.8063	0.7198	0.5903	0.2631
	TNN	0.9951	**0.9853**	0.9625	0.9244	0.8599	0.7620	0.6295	0.4220
	3DLogTNN	0.9064	0.8963	0.8851	0.8723	0.8501	0.8121	0.7289	0.4814
	METNN	0.9951	0.9869	0.9686	0.9379	0.8765	0.7868	0.6553	0.3463
	TRLRF	0.9852	0.9729	0.9508	0.9161	0.8530	0.7687	0.6525	0.4933
	TRGFR	**0.9954**	**0.9902**	**0.9811**	**0.9667**	**0.9405**	**0.8915**	**0.8066**	**0.6349**
	FCTN	0.9767	0.9578	0.9235	0.8806	0.8243	0.7073	0.5438	0.3363
	FCTNFR	**0.9971**	**0.9923**	**0.9818**	**0.9629**	**0.9253**	**0.8649**	**0.7863**	**0.6207**
	FCTNGS	0.9781	0.9609	0.9257	0.8922	0.8250	0.7332	0.6308	0.4409
	FCTN-FDS	**0.9970**	**0.9923**	**0.9832**	**0.9642**	**0.9308**	**0.8780**	**0.7963**	**0.6425**

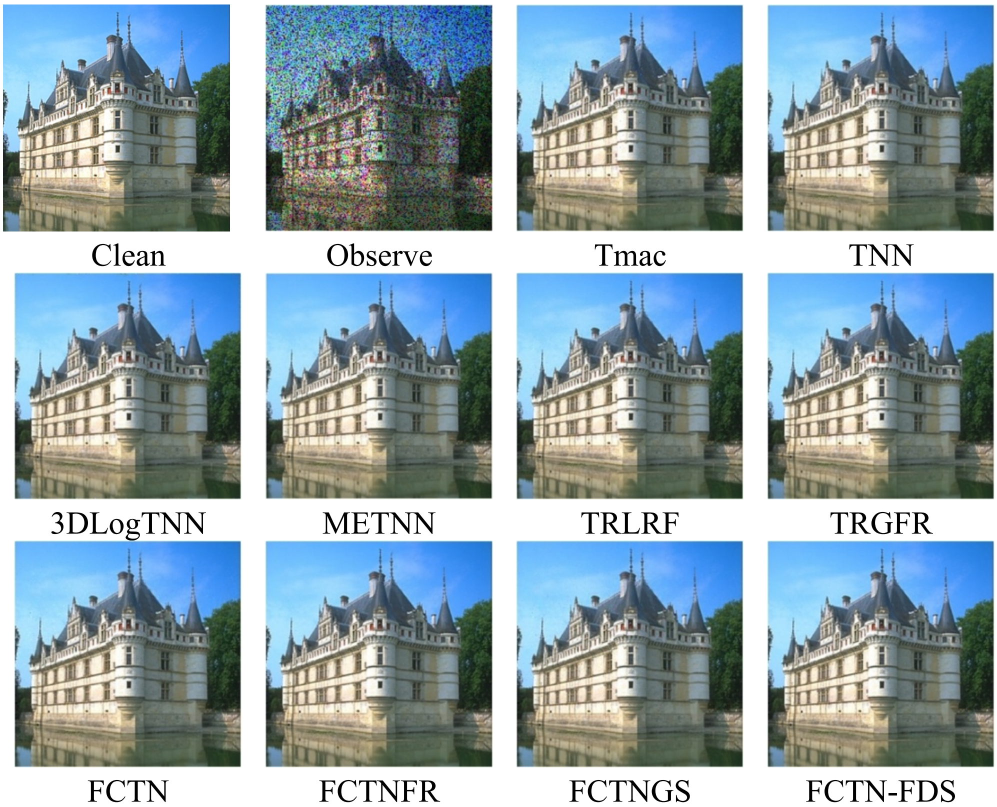

Figure 3. Visual results of “Castle” at MR = 30%.

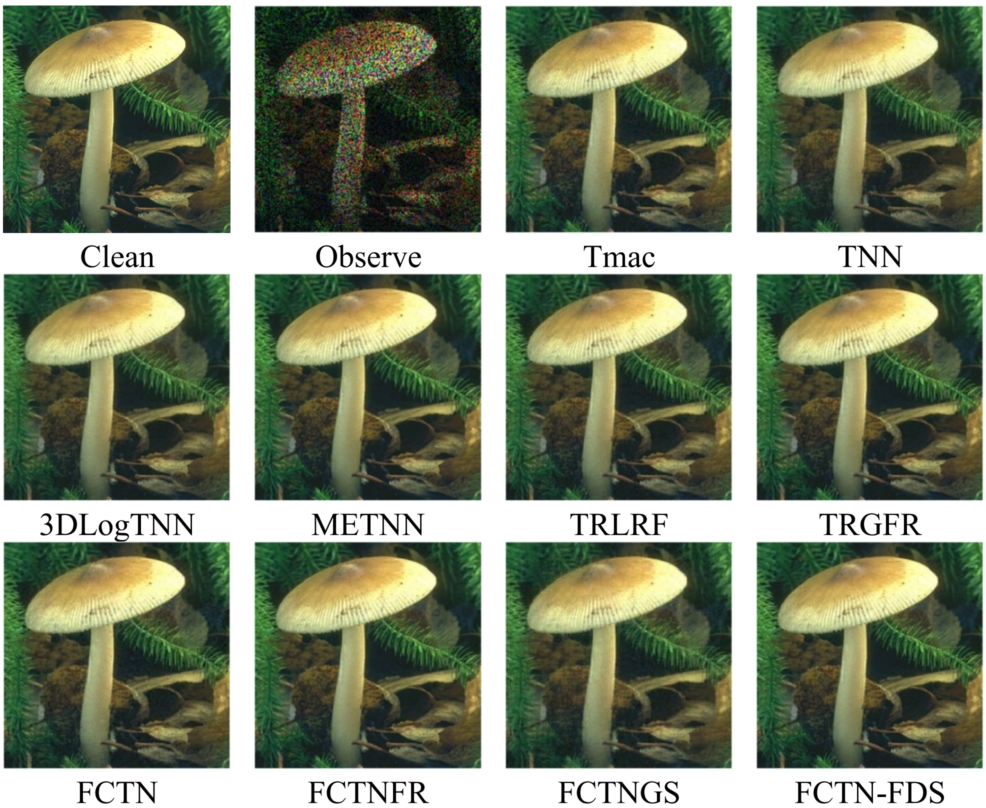

Figure 4. Visual results of “Mushroom” at MR = 50%.

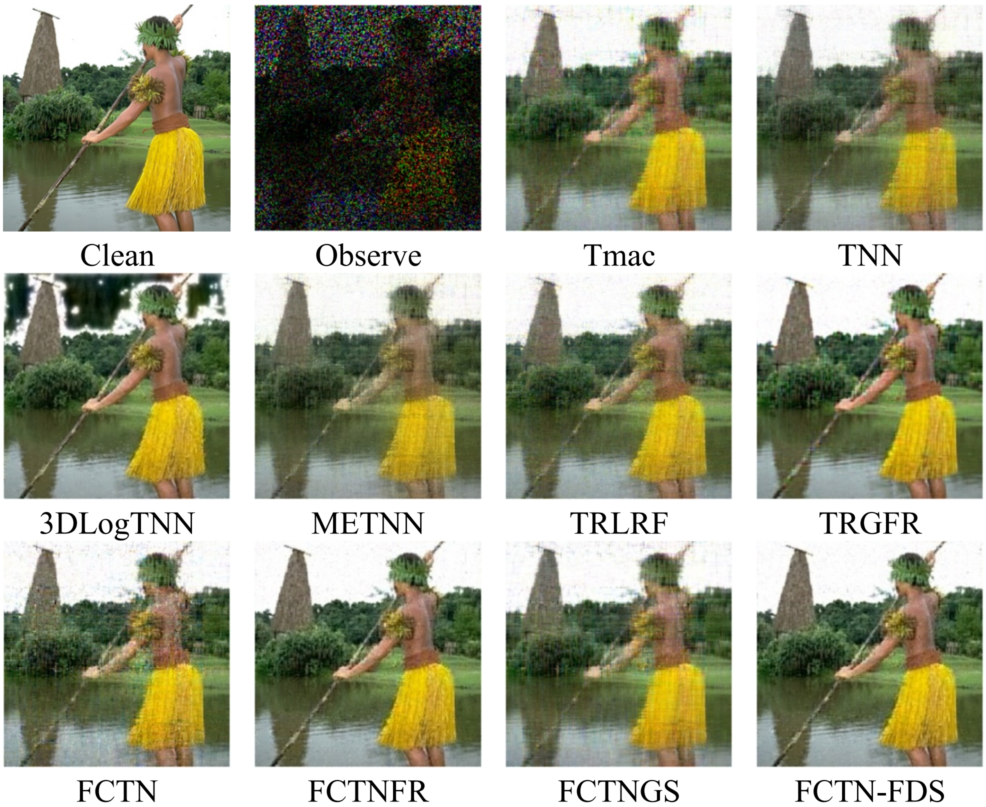

Figure 5. Visual results of “Human” at MR = 80%.

For better visual comparison, the reconstruction visual effects of “Castle” at MR = 30%, “Mushroom” at MR = 50%, and “Human” at MR = 80% are exhibited in Figures 3–5, respectively. It can be observed that the proposed FCTN-FDS can recover the global structure while well preserving the local detailed textures and image colors under different missing rates. Therefore, the proposed method delivers favorable visual reconstruction performance.

4.2.2. Graffiti removal application

In the context of graffiti removal, we present the experimental results of three color-image-based graffiti removal methods (Steeple, Pottery, Water). Figures 6–8 display the visual reconstruction results for “Steeple” with alphabet doodles, “Pottery” with irregular doodles, and “Water” with mesh doodles, respectively. Experiments demonstrate that FCTN-FDS provides a significant advantage in subjective quality. For the “Water” image, the proposed method effectively recovers complex natural textures while avoiding the blurring artifacts common to other methods. The “Steeple” image exhibits the strongest edge-preserving ability, yielding the clearest and sharpest architectural structures. Overall, FCTN-FDS achieves superior visual consistency and detail restoration for images with complex structures and rich textures. Table 4 presents the quantitative restoration results (PSNR and SSIM) for the graffiti removal task. In the table, the optimal, suboptimal, and third-best algorithm performance values are marked in red bold, blue bold, and green bold fonts, respectively. Combined with quantitative and qualitative analysis, the proposed FCTN-FDS method achieves the overall best comprehensive performance. FCTN-FDS achieves the highest PSNR and SSIM values in the Steeple and Water test cases, demonstrating its strong ability to restore fine details and natural textures. In the

Pottery test case, although FCTN-FDS does not rank first in PSNR and SSIM, it maintains high reconstruction quality. Overall, the FCTN-FDS method exhibits excellent robustness and restoration performance in most scenarios.

Table 4. Quantitative analysis of doodle removal applications.

Method	Steeple		Pottery		Water	
	PSNR	SSIM	PSNR	SSIM	PSNR	SSIM
Tmac	23.90	0.8272	19.86	0.7094	25.51	0.8147
TNN	27.73	**0.8791**	**29.31**	**0.8264**	**28.12**	**0.8644**
3DLogTNN	14.42	0.5382	10.95	0.4794	13.85	0.6057
METNN	27.43	**0.8863**	26.34	0.7894	**28.33**	0.8717
TRLRF	**28.33**	0.8755	**29.41**	**0.8175**	27.93	**0.8518**
TRGFR	23.10	0.8413	19.36	0.7161	24.17	0.8224
FCTN	24.74	0.8127	25.91	0.7476	24.49	0.8074
FCTNFR	**28.07**	0.8592	24.72	0.7752	25.03	0.8250
FCTNGS	28.03	0.8617	**28.94**	**0.8189**	26.24	0.8313
FCYN-FDS	**30.12**	**0.8947**	27.45	0.8098	**28.41**	**0.8697**

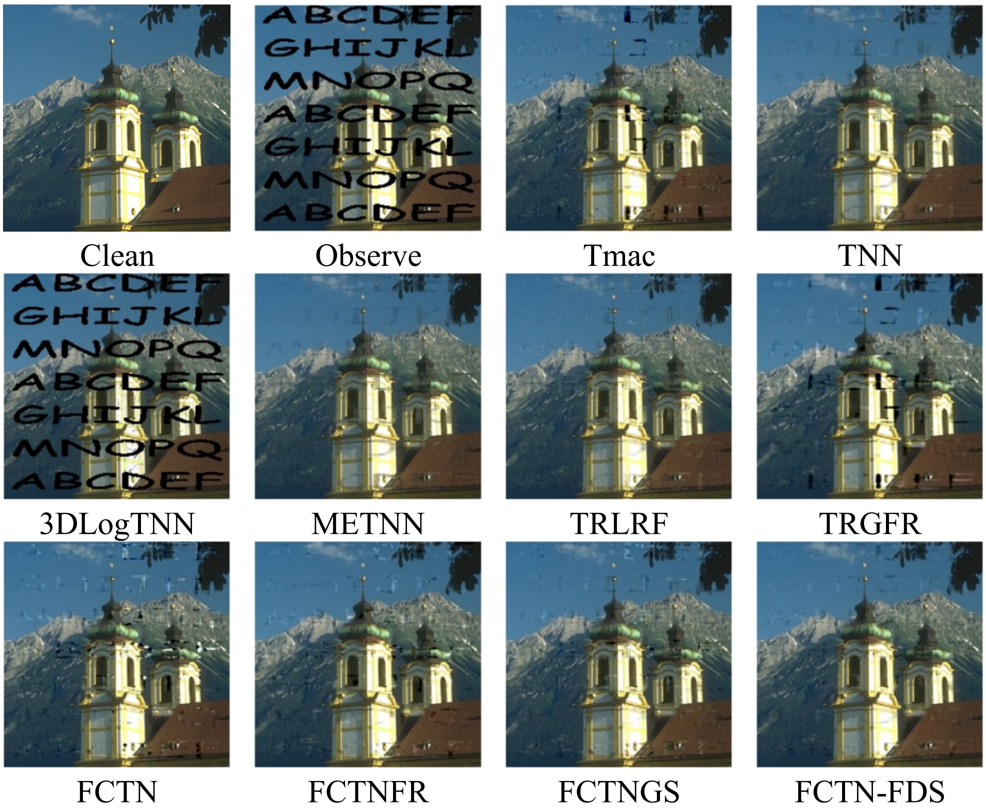

Figure 6. Visual results of "Steeple" with alphabet doodles.

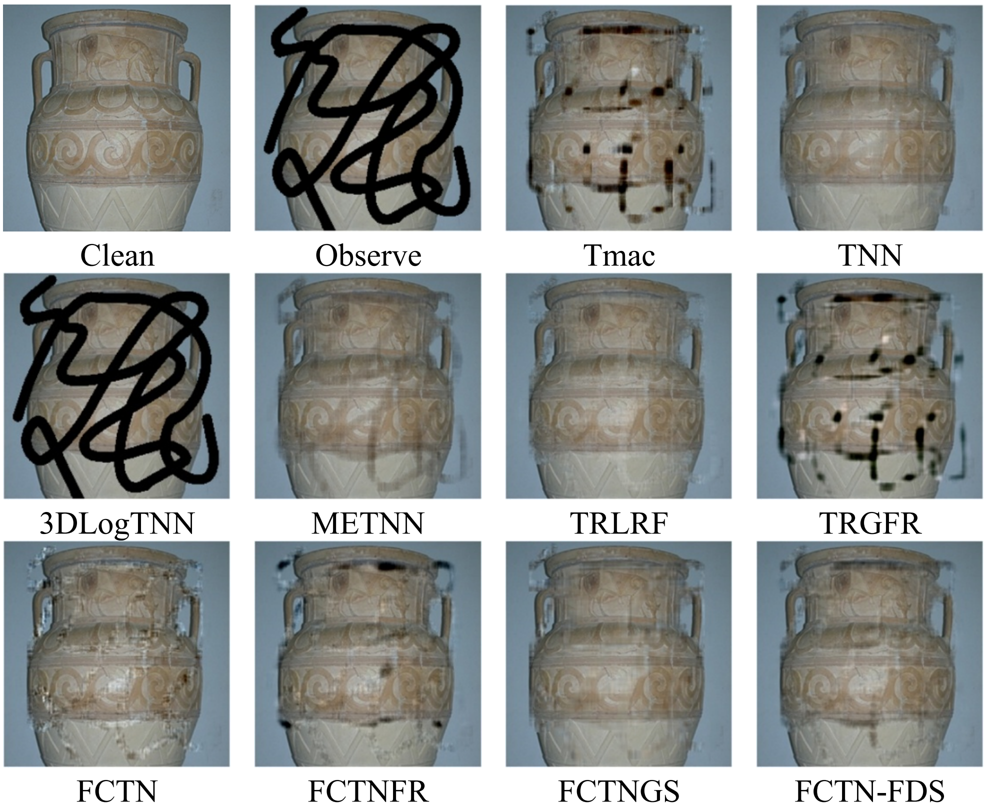

Figure 7. Visual results of “Pottery” with irregular doodles.

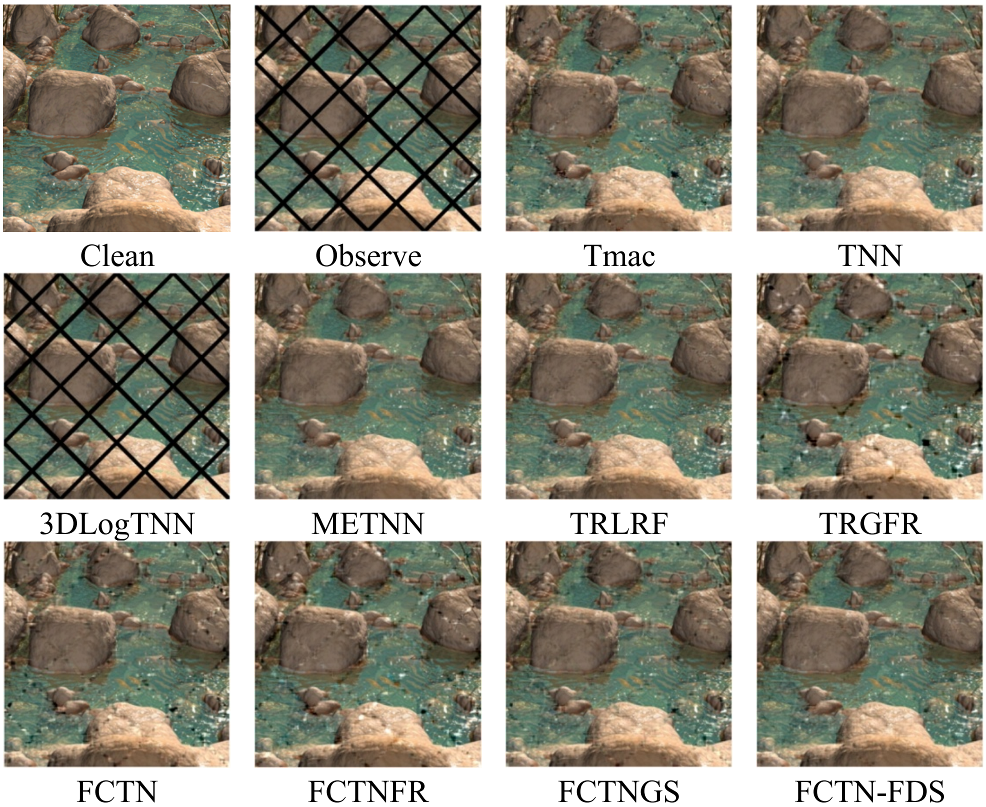

Figure 8. Visual results of “Water” with mesh doodles.

4.3. Multispectral image completion

In this subsection, we evaluate the robustness of various methods under the extreme condition of an 80% high-missing rate in the multispectral image "Beers". The number of iterations is set to 100. As shown in the visual reconstruction results in Figure 9, 3DLogTNN, FCTN-FDS, and FCTNFR demonstrate superior reconstruction capabilities. They significantly outperform other methods in recovering the beer glass's transparent texture, the color fidelity of the color checker, and overall structural integrity. Regarding FCTN-FDS and FCTNFR, although their visual effects are similar, a careful comparison of the residual images at the bottom reveals that FCTN-FDS produces fewer artifacts, particularly at the glass edges and color checker details. This indicates that the structural sparse constraint introduced in FCTN-FDS plays a positive role in further optimizing detail fidelity, enabling more precise recovery of subtle textures and spectral consistency. In summary, FCTN-FDS exhibits reconstruction performance comparable to, or even slightly better than, FCTNFR in handling multispectral images with high missing rates, validating the effectiveness of the proposed model in processing complex spectral data.

4.4. MRI image completion

In this section, we conduct reconstruction experiments on brain MRI images with a high missing rate of 80%, using the 90th band for visual presentation. The maximum number of iterations is set to 100. By comparing the visual results and residual images of different algorithms, the performance of the FCTN-FDS method in medical image inpainting is systematically evaluated. As can be observed in Figure 10, the 3DLogTNN, FCTN-FDS, and FCTNFR methods achieve superior reconstruction performance with remarkable visual quality, successfully recovering the fine structural details of brain tissues, including the boundaries of gray matter and white matter, the textures of cerebral gyri and sulci, and the contour of the skull. The reconstructed images are clear overall, with no obvious artifacts.

In contrast, the Tmac method suffers from severe block artifacts and structural distortion in missing regions. The TNN method can preserve only the general outline while blurring fine details and retaining noticeable noise residuals. The METNN method causes over-smoothing within brain tissues, leading to the loss of texture details. Although TRLRF and TRGFR can partially restore structural information, they suffer from insufficient edge sharpness and slight color deviations. Although FCTN-FDS delivers an overall performance highly comparable to FCTNFR, with both maintaining extremely low levels of residual images, a detailed comparison reveals that FCTN-FDS produces fewer noise responses in the texture regions of brain tissues and achieves purer edge details. In conclusion, FCTN-FDS exhibits state-of-the-art reconstruction capability comparable to FCTNFR and outperforms it in detail preservation when handling medical images with a high missing rate, thereby verifying the effectiveness and robustness of the proposed model for complex medical image inpainting tasks.

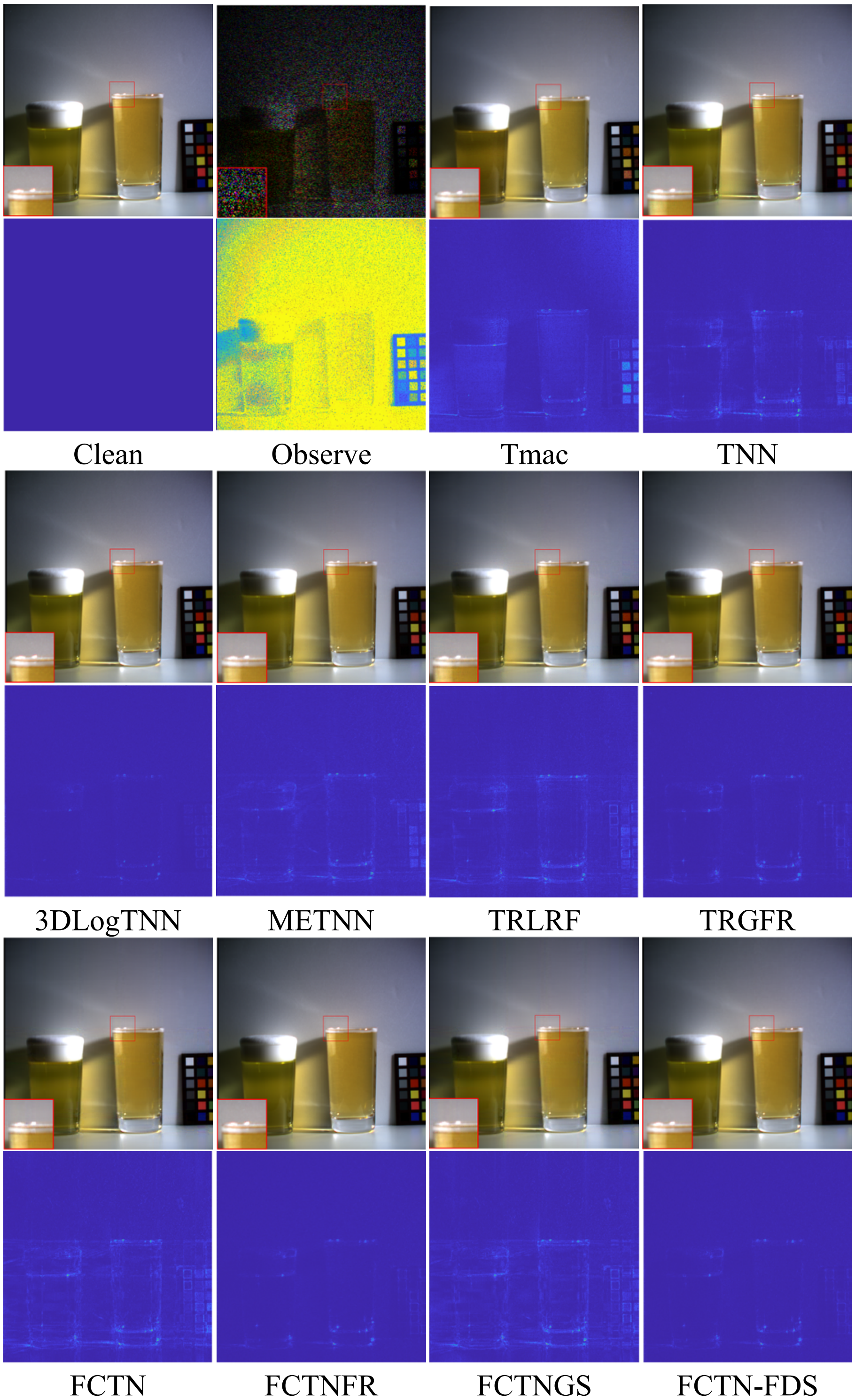

Figure 9. Visual reconstruction results and corresponding residual images of the multispectral image “Beers” at MR = 80%.

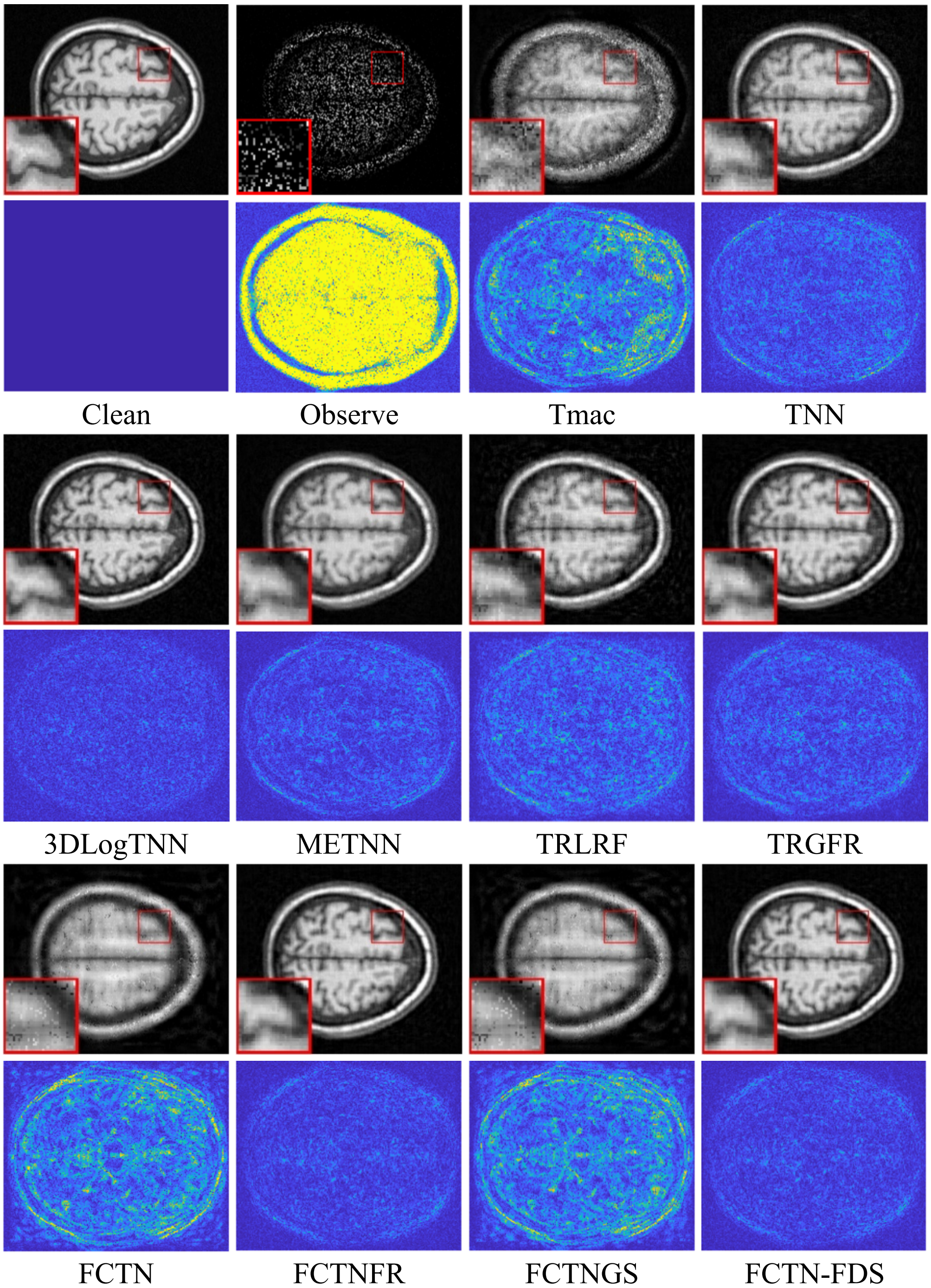

Figure 10. Visual reconstruction results and corresponding residual images of the MRI image at MR = 80%.

4.5. Convergence analysis

Figure 11 presents the PSNR convergence curves of different methods on various color images (Castle, Mushroom, Human, Steeple, Pottery, Water) under a high missing rate of 90%. In terms of the overall trend, all methods exhibit a consistent convergence characteristic: The PSNR value rises rapidly with increasing iteration numbers and then stabilizes. Among all competitors, the proposed FCTN-FDS method (red curve) achieves the fastest convergence speed and the highest final PSNR value for most test images, demonstrating stronger robustness and reconstruction capability for image recovery under high missing rates. By comparison, FCTNFR (blue curve) and FCTNGS (green curve) can also attain relatively high PSNR values on partial images. Yet, their convergence speed and final quantitative accuracy are slightly inferior to those of FCTN-FDS. In addition, the baseline FCTN method (black curve) shows mediocre performance across all test images, further verifying the significance of introducing structural sparse constraints and gradient factor regularization for performance improvement. In summary, FCTN-FDS not only outperforms other methods in visual quality but also demonstrates remarkable superiority in quantitative metrics and convergence efficiency, demonstrating its effectiveness and superiority in image inpainting tasks with high missing rates. For the detailed proof of convergence, please refer to [33].

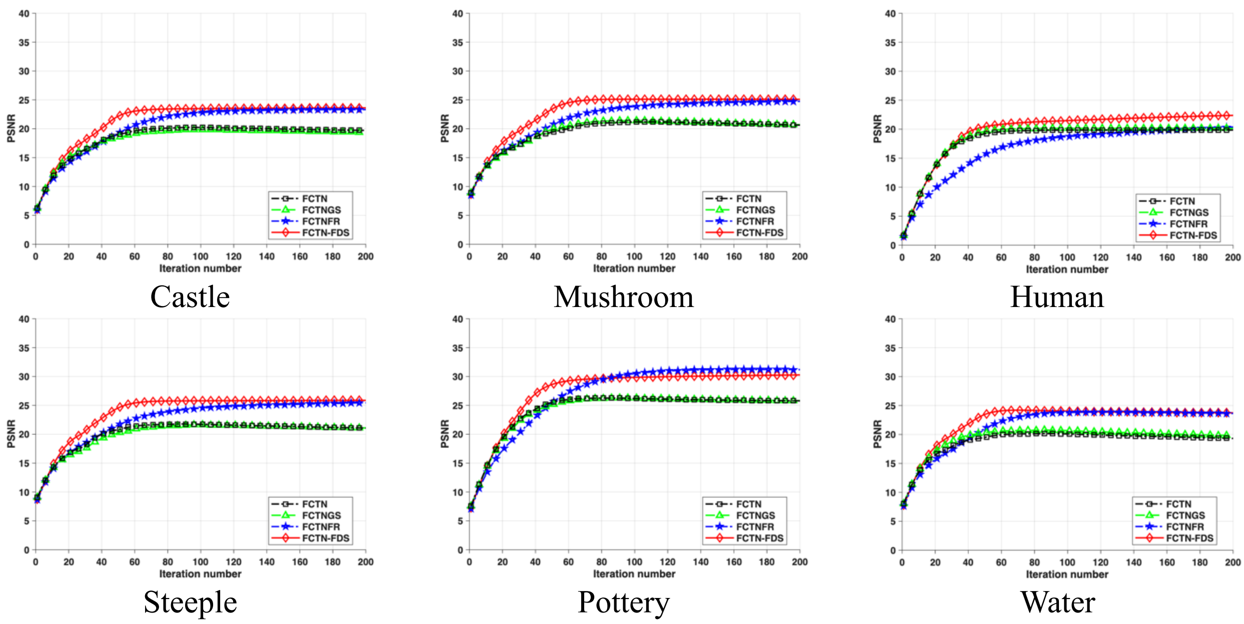

Figure 11. PSNR convergence curves of various methods for color images at MR = 90%.

4.6 Ablation study

To evaluate the individual contributions of gradient factor regularization and structural sparse regularization, in this subsection, we assess the performance of four variants: FCTN (baseline), FCTN-GS (incorporating structural sparse regularization), FCTN-FR (incorporating gradient factor regularization), and FCTN-FDS (incorporating both gradient factor and structural sparse regularization).

In Figure 12, we present the PSNR and SSIM bar charts for the color image "Human" under missing rates (MR) of 70%, 80%, and 90%. Our results indicate that across all missing rates, the three reconstruction methods achieve varying degrees of improvement in PSNR and SSIM values compared to the baseline algorithm, FCTN. For example, with PSNR, FCTN-GS improves upon the baseline by 0.50 dB to 1.35 dB. FCTN-FR yields a more significant gain, with improvements ranging from 3.85 dB to 4.34 dB. The proposed FCTN-FDS achieves the highest performance, with PSNR gains ranging from 4.21 dB to 4.52 dB over the baseline. These results suggest that introducing gradient factor regularization and structural sparse regularization into the FCTN framework effectively induces the sparsity of the factor tensor, thereby enhancing the robustness of rank selection and enabling the recovery of finer details and textures. Furthermore, since FCTN-FDS outperforms FCTN-FR and FCTN-GS, the combined effect of the two regularization terms proves beneficial, validating the effectiveness of the proposed FCTN-FDS.

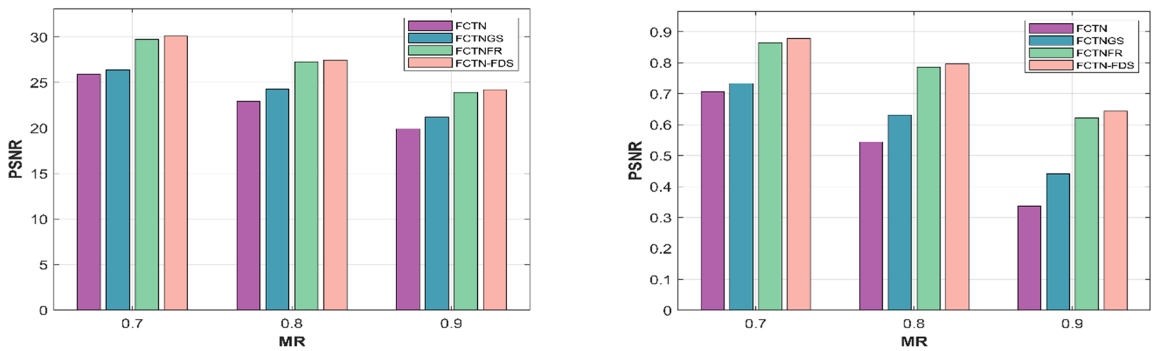

Figure 12. Impact of gradient factor regularization and structural sparse regularization on model performance for the "Human" image under varying MR conditions.

4.7. Parameter sensitivity analysis

In this section, we analyze the sensitivity of the FCTN-FDS method to parameters λ_k, β_k, and μ_k. Parameter λ_k is selected from 0.0001 to 0.1, while parameter β_k is chosen from 0.001 to 1, and μ_k is chosen from 0.05 to 7.

Table 5. The impact of λ_k on the PSNR values of the color images Castle, Mushroom, and Human under the condition of MR = 60%.

Picture	λ_k						
	0.0001	0.0005	0.001	0.005	0.01	0.05	0.1
Castle	32.25	32.28	32.28	32.30	32.27	32.55	32.49
Mushroom	34.06	34.07	34.10	34.16	34.15	34.25	34.30
Human	32.55	32.70	32.66	32.68	32.74	32.81	32.87

Table 5 presents the performance of the FCTN-FDS method under various values of parameter λ_k when MR = 60%. It can be observed that the proposed method exhibits low sensitivity to parameter λ_k. Consequently, we set $\lambda_k = 0.1$ for the color image completion experiments. Specifically, the fluctuation ranges of PSNR are merely within 0.3 dB, 0.24 dB, and 0.32 dB for the test images Castle, Mushroom, and Human, respectively. These statistical results demonstrate the robustness of the FCTN-

FDS method with respect to parameter λ_k.

Table 6 presents the performance of the FCTN-FDS method under varying values of parameter β_k with MR = 60%. It can be observed that the FCTN-FDS method exhibits low sensitivity to parameter β_k. Consequently, we set $\beta_k = 0.5$ for the color image completion experiments. The PSNR fluctuations remain within 0.96 dB, 0.81 dB, and 0.85 dB for the test images Castle, Mushroom, and Human, respectively. Statistical results confirm that the FCTN-FDS method maintains highly stable performance regardless of variations in parameter β_k.

Table 6. The impact of β_k on the PSNR values of the color images Castle, Mushroom, and Human when MR = 60%.

Picture	β_k						
	0.001	0.005	0.01	0.05	0.1	0.5	1
Castle	31.63	31.59	31.69	31.85	31.97	32.49	32.55
Mushroom	33.49	33.54	33.62	33.85	34.01	34.30	34.26
Human	32.05	32.11	32.03	32.21	32.41	32.87	32.88

Table 7 presents the performance of the FCTN-FDS method under varying values of parameter μ_k with MR = 60%. It can be observed that the FCTN-FDS method exhibits low sensitivity to parameter μ_k. Consequently, we set $\mu_k = 1$ for the color image completion experiments. The fluctuation ranges of PSNR are merely within 1.37 dB, 1.94 dB, and 1.45 dB for the test images Castle, Mushroom, and Human, respectively. Our results confirm that the performance of the FCTN-FDS method remains stable regardless of variations in parameter μ_k.

Table 7. The impact of μ_k on the PSNR values of the color images Castle, Mushroom, and Human when MR = 60%.

Picture	μ_k						
	0.05	0.1	0.5	1	3	5	7
Castle	32.10	32.50	32.55	32.49	31.86	31.35	31.18
Mushroom	34.01	34.20	34.25	34.30	33.39	32.70	32.36
Human	32.41	32.77	32.85	32.87	32.13	31.60	31.42

5. Conclusions

In this paper, we propose a novel FCTN decomposition method based on factor-double-sparse constraint regularization, termed FCTN-FDS. By introducing gradient factor regularization and structural sparse regularization within the FCTN framework, this method promotes the sparsity of factor tensors from two perspectives: The factors themselves and the network structure. Furthermore, it enhances the robustness of rank selection by adaptively pruning near-zero groups. Based on the proposed decomposition, we design a corresponding tensor completion model and solve it using the PAM algorithm. Extensive experiments on third-order datasets, including color, multispectral, and MRI images, validate the effectiveness of FCTN-FDS. However, there is room for improvement in two aspects. On one hand, the parameters of FCTN-FDS require time-consuming manual tuning. On the other hand, despite its superior performance in image restoration, the high computational cost remains a significant issue. In future work, we aim to introduce modules that adaptively select parameters to reduce the burden of manual tuning. Additionally, we will explore more efficient solvers to lower computational costs, thereby improving the method's practicality and extending its application to higher-dimensional data.

Use of AI tools declaration

The authors declare they have not used Artificial Intelligence (AI) tools in the creation of this article.

Acknowledgments

This work was supported by the Natural Science Foundation of Fujian Province (2024J01820, 2024J01821, 2024J01822, 2026J002035), the Principal Foundation of Minnan Normal University (KJ19019), Postgraduate Education and Teaching Reform Research Project (YJG202526), the High-Level Science Research Project of Minnan Normal University (GJ19019), National Independent Innovation Demonstration Zone System (Fuzhou, Xiamen, Quanzhou) Innovation Platform Project (3502ZCQXT2024006),, and Major Postgraduate Education Reform Project of Undergraduate Colleges and Universities in Fujian Province (FBJY20250180).

Conflict of interest

The authors declare there is no conflict of interest.

References

1. X. Su, H. Ge, Z. Liu, Y. Shen, Low-rank tensor completion based on nonconvex regularization, *Signal Process.*, **212** (2023), 109157. https://doi.org/10.1016/j.sigpro.2023.109157
2. S. Lu, P. Wang, W. Zhu, C. Dai, Y. Zhang, C. Liu, et al., A nonlocal feature self-similarity based tensor completion method for video recovery, *Neurocomputing*, **580** (2024), 127513. https://doi.org/10.1016/j.neucom.2024.127513

3. N. D. Sidiropoulos, L. De Lathauwer, X. Fu, K. Huang, E. E. Papalexakis, C. Faloutsos, Tensor decomposition for signal processing and machine learning, *IEEE Trans. Signal Process.*, **65** (2017), 3551–3582. https://doi.org/10.1109/TSP.2017.2690524
4. A. Cichocki, D. Mandic, L. De Lathauwer, G. Zhou, Q. Zhao, C. Caiafa, et al., Tensor decompositions for signal processing applications: From two-way to multiway component analysis, *IEEE Signal Process. Mag.*, **32** (2015), 145–163. https://doi.org/10.1109/MSP.2013.2297439
5. W. H. Wu, T. Z. Huang, H. Zhang, J. L. Wang, X. L. Zhao, Untrained low-rank neural network prior for multi-dimensional image recovery, *IEEE Signal Process. Lett.*, **30** (2023), 1647–1651. https://doi.org/10.1109/LSP.2023.3325673
6. Y. T. Zhao, W. F. Cao, Y. Chen, Local-and-nonlocal spectral prior regularized tensor recovery for cauchy noise removal, *Signal Process.*, **213** (2023), 109176. https://doi.org/10.1016/j.sigpro.2023.109176
7. B. D. Haeffele, R. Vidal, Structured low-rank matrix factorization: Global optimality, algorithms, and applications, *IEEE Trans. Pattern Anal. Mach. Intell.*, **42** (2019), 1468–1482. https://doi.org/10.1109/TPAMI.2019.2900306
8. P. L. Wu, X. L. Zhao, M. Ding, Y. B. Zheng, L. B. Cui, T. Z. Huang, Tensor ring decomposition-based model with interpretable gradient factors regularization for tensor completion, *Knowl.-Based Syst.*, **259** (2023), 110094. https://doi.org/10.1016/j.knosys.2022.110094
9. Z. Zha, X. Yuan, J. Zhou, C. Zhu, B. Wen, Image restoration via simultaneous nonlocal self-similarity priors, *IEEE Trans. Image Process.*, **29** (2020), 8561–8576. https://doi.org/10.1109/TIP.2020.3015545
10. Y. Chen, Y. Liao, Y. He, X. He, Q. Yu, T. Chen, et al., Non-local similar block matching and hybrid low-rank tensor network for colour image inpainting, *Digit. Signal Process.*, **162** (2025), 105169. https://doi.org/10.1016/j.dsp.2025.105169
11. T. G. Kolda, B. W. Bader, Tensor decompositions and applications, *SIAM Rev.*, **51** (2009), 455–500. https://doi.org/10.1137/07070111X
12. M. E. Kilmer, L. Horesh, H. Avron, E. Newman, Tensor-tensor algebra for optimal representation and compression of multiway data, *Proc. Natl. Acad. Sci.*, **118** (2021), e2015851118. https://doi.org/10.1073/pnas.2015851118
13. M. Ding, X. Fu, T. Z. Huang, J. Wang, X. L. Zhao, Hyperspectral super-resolution via interpretable block-term tensor modeling, *IEEE J. Sel. Top. Signal Process.*, **15** (2020), 641–656. https://doi.org/10.1109/JSTSP.2020.3045965
14. N. Vervliet, O. Debals, L. Sorber, L. De Lathauwer, Breaking the curse of dimensionality using decompositions of incomplete tensors: Tensor-based scientific computing in big data analysis, *IEEE Signal Process. Mag.*, **31** (2014), 71–79. https://doi.org/10.1109/MSP.2014.2329429
15. W. Jiang, J. Zhang, C. Zhang, L. Wang, H. Qi, Robust low tubal rank tensor completion via factor tensor norm minimization, *Pattern Recognit.*, **135** (2023), 109169. https://doi.org/10.1016/j.patcog.2022.109169
16. W. Kong, F. Zhang,W. Qin, J. Wang, Low-tubal-rank tensor recovery with multilayer subspace prior learning, *Pattern Recognit.*, **140** (2023), 109545. https://doi.org/10.1016/j.patcog.2023.109545

17. T. Liao, Z. Wu, C. Chen, Z. Zheng, X. Zhang, Tensor completion via convolutional sparse coding with small samples-based training, *Pattern Recognit.*, **141** (2023), 109624. https://doi.org/10.1016/j.patcog.2023.109624
18. S. Yuan, K. Huang, A generalizable framework for low-rank tensor completion with numerical priors, *Pattern Recognit.*, **155** (2024), 110678. https://doi.org/10.1016/j.patcog.2024.110678
19. X. Li, Y. Ye, X. Xu, Low-rank tensor completion with total variation for visual data inpainting, in *Proceedings of the AAAI Conference on Artificial Intelligence*, AAAI Press, (2017), 2210–2216. https://doi.org/10.1609/aaai.v31i1.10776
20. Y. Wang, J. Peng, Q. Zhao, Y. Leung, X. L. Zhao, D. Meng, Hyperspectral image restoration via total variation regularized low-rank tensor decomposition, *IEEE J. Sel. Top. Appl. Earth Obs. Remote Sens.*, **11** (2017), 1227–1243. https://doi.org/10.1109/JSTARS.2017.2779539
21. R. A. Harshman, Foundations of the parafac procedure: Models and conditions for an "explanatory" multi-modal factor analysis, *UCLA Work. Pap. Phon.*, **16** (1970), 84.
22. J. D. Carroll, J. J. Chang, Analysis of individual differences in multidimensional scaling via an n-way generalization of "eckart-young" decomposition, *Psychometrika*, **35** (1970), 283–319. https://doi.org/10.1007/BF02310791
23. L. R. Tucker, Some mathematical notes on three-mode factor analysis, *Psychometrika*, **31** (1966), 279–311. https://doi.org/10.1007/bf02289464
24. C. J. Hillar, L. H. Lim, Most tensor problems are np-hard, *J. ACM*, **60** (2013), 1–39. https://doi.org/10.1145/2512329
25. A. Cichocki, N. Lee, I. Oseledets, A. H. Phan, Q. Zhao, D. P. Mandic, Tensor networks for dimensionality reduction and large-scale optimization part 1 low-rank tensor decompositions, *Found. Trends Mach. Learn.*, **9** (2016), 249–429. https://doi.org/10.1561/2200000059
26. A. Cichocki, A. H. Phan, Q. Zhao, N. Lee, I. Oseledets, M. Sugiyama, et al., Tensor networks for dimensionality reduction and large-scale optimizations part 2 applications and future perspectives, *Found. Trends Finance*, **9** (2017), 431–673. https://doi.org/10.1561/2200000067
27. A. Cichocki, Era of big data processing: A new approach via tensor networks and tensor decompositions, preprint, arXiv:1403.2048.
28. C. Li, Z. Sun, Evolutionary topology search for tensor network decomposition, in *Proceedings of the 37th International Conference on Machine Learning*, Cambridge, PMLR, (2020), 5947–5957.
29. I. V. Oseledets, Tensor-train decomposition, *SIAM J. Sci. Comput.*, **33** (2011), 2295–2317. https://doi.org/10.1137/090752286
30. Q. Zhao, G. Zhou, S. Xie, L. Zhang, A. Cichocki, Tensor ring decomposition, preprint, arXiv:1606.05535.
31. Y. Chen, P. Zhuo, H. Zhang, Y. Liao, Z. Chen, R. Zhang, et al., Tensor ring decomposition with data-driven for color image completion, *Electron. Res. Arch.*, **34** (2026), 477–508. https://doi.org/10.3934/era.2026023
32. Y. B. Zheng, T. Z. Huang, X. L. Zhao, Q. Zhao, T. X. Jiang, Fully-connected tensor network decomposition and its application to higher-order tensor completion, in *Proceedings of the AAAI Conference on Artificial Intelligence*, AAAI Press, (2021), 11071–11078. https://doi.org/10.1609/aaai.v35i12.17321
33. Y. B. Zheng, T. Z. Huang, X. L. Zhao, Q. Zhao, Tensor completion via fully-connected tensor network decomposition with regularized factors, *J. Sci. Comput.*, **92** (2022), 8. https://doi.org/10.1007/s10915-022-01841-8

34. W. J. Huang, L. Huang, T. X. Jiang, Y. B. Zheng, G. Liu, Efficient fctn decomposition with structural sparsity for noisy tensor completion, *IEEE Trans. Big Data*, **11** (2025), 3225–3239. https://doi.org/10.1109/TBDATA.2025.3588029
35. J. Liu, C. Zhu, Y. Liu, Smooth compact tensor ring regression, *IEEE Trans. Knowl. Data Eng.*, **34** (2022), 4439–4452. https://doi.org/10.1109/tkde.2020.3037131
36. Y. Xu, R. Hao, W. Yin, Z. Su, Parallel matrix factorization for low-rank tensor completion, *Inverse Probl. Imaging*, **9** (2015), 601–624. https://doi.org/10.3934/ipi.2015.9.601
37. Q. Zhao, G. Zhou, S. Xie, L. Zhang, A. Cichocki, Tensor ring decomposition, preprint, arXiv:1606.05535.
38. S. Liu, X. L. Zhao, J. Leng, B. Z. Li, J. H. Yang, X. Chen, Revisiting high-order tensor singular value decomposition from basic element perspective, *IEEE Trans. Signal Process.*, **72** (2024), 4589–4603. https://doi.org/10.1109/TSP.2024.3454115
39. Y. B. Zheng, T. Z. Huang, X. L. Zhao, T. X. Jiang, T. H. Ma, T. Y. Ji, Mixed noise removal in hyperspectral image via low-fibered-rank regularization, *IEEE Trans. Geosci. Remote Sens.*, **58** (2019), 734–749. https://doi.org/10.1109/TGRS.2019.2940534
40. L. Yuan, C. Li, D. Mandic, J. Cao, Q. Zhao, Tensor ring decomposition with rank minimization on latent space: An efficient approach for tensor completion, in *Proceedings of the AAAI Conference on Artificial Intelligence*, AAAI Press, (2019), 9151–9158. https://doi.org/10.1609/aaai.v33i01.33019151